

Comparing galaxy formation in semi-analytic models and hydrodynamical simulations

Peter D. Mitchell¹*, Cedric G. Lacey², Claudia D. P. Lagos³, Carlos S. Frenk², Richard G. Bower², Shaun Cole², John C. Helly², Matthieu Schaller², Violeta Gonzalez-Perez⁴, Tom Theuns^{2,5}

¹Univ Lyon, Univ Lyon1, Ens de Lyon, CNRS, Centre de Recherche Astrophysique de Lyon UMR5574, F-69230, Saint-Genis-Laval, France

²Institute for Computational Cosmology, Department of Physics, University of Durham, South Road, Durham, DH1 3LE, UK

³International Centre for Radio Astronomy Research, 7 Fairway, Crawley, 6009, Perth, WA, Australia

⁴Institute of Cosmology and Gravitation, Portsmouth University, Dennis Sciama Building, Burnaby Road, Portsmouth PO1 3FX, UK

⁵Department of Physics, University of Antwerp, Groenenborgerlaan 171, B-2020 Antwerpen, Belgium

18 May 2022

ABSTRACT

It is now possible for hydrodynamical simulations to reproduce a representative galaxy population. Accordingly, it is timely to assess critically some of the assumptions of traditional semi-analytic galaxy formation models. We use the EAGLE simulations to assess assumptions built into the GALFORM semi-analytic model, focussing on those relating to baryon cycling, angular momentum and feedback. We show that the assumption in GALFORM that newly formed stars have the same specific angular momentum as the total disc leads to a significant overestimate of the total stellar specific angular momentum of disc galaxies. In EAGLE, stars form preferentially out of low specific angular momentum gas in the interstellar medium (ISM) due to the assumed gas density threshold for stars to form, leading to more realistic galaxy sizes. We find that stellar mass assembly is similar between GALFORM and EAGLE but that the evolution of gas properties is different, with various indications that the rate of baryon cycling in EAGLE is slower than is assumed in GALFORM. Finally, by matching individual galaxies between EAGLE and GALFORM, we find that an artificial dependence of AGN feedback and gas infall rates on halo mass doubling events in GALFORM drives most of the scatter in stellar mass between individual objects. Put together our results suggest that the GALFORM semi-analytic model can be significantly improved in light of recent advances.

Key words: galaxies: formation – galaxies: evolution – galaxies: haloes – galaxies: stellar content

1 INTRODUCTION

Semi-analytic galaxy formation models are established tools for connecting the predicted hierarchical growth of dark matter haloes to the observed properties of the galaxy population (e.g. Cole et al. 2000; Somerville et al. 2008b; Guo et al. 2011). Unlike empirical abundance matching (e.g. Conroy et al. 2006; Moster et al. 2010) or halo occupation distribution models (e.g. Berlind & Weinberg 2002), semi-analytic models employ a forward-modelling approach and are constructed such that they contain as much as possible of the baryonic physics that is thought to be relevant to galaxy evolution, albeit at a simplified, macroscopic level. The simplified, macroscopic nature of semi-analytic models means that they are

computationally inexpensive to evaluate. Compared to hydrodynamical simulations, this lack of computational expense meant that until recently it was uniquely possible for semi-analytic models to predict realistic galaxy populations (e.g. Bower et al. 2006; Croton et al. 2006; Henriques et al. 2013).

Recently, advances in computational resources combined with improvements in the uncertain modelling of feedback have allowed hydrodynamical simulations to predict galaxy populations which reproduce observations at an equivalent level to semi-analytic models for representative volumes (Vogelsberger et al. 2014; Schaye et al. 2015; Dubois et al. 2014; Davé et al. 2016). It is timely therefore to review the underling assumptions which underpin semi-analytic models and assess their validity against state-of-the-art hydrodynamical simulations.

As in semi-analytic models, hydrodynamical simulations are forced to implement uncertain subgrid modelling to approximate

* E-mail: peter.mitchell@univ-lyon1.fr

the effect of massive stars and black holes on galaxy evolution. This means that, for example, the dynamics of outflowing gas in these simulations are not necessarily realistic (irrespective of whether a realistic galaxy population is produced). Importantly however, the dynamics of outflows are tracked self-consistently in hydrodynamical simulations. Furthermore, simulations do not need to make any assumptions regarding angular momentum conservation of the various baryonic components of galaxies and their surrounding gas flows. In semi-analytic models, both these aspects of galaxy evolution are among the most important for predicting galaxy properties and yet are also among the most uncertain (Henriques et al. 2013; Mitchell et al. 2014; Hirschmann et al. 2016). Arguably therefore, the parametrisations of these physical processes that are implemented in semi-analytic models should be capable of reproducing (with an appropriate choice of model parameters) the behaviour predicted by hydrodynamical simulations. Here, we begin to address this topic by comparing the properties of galaxies between the established semi-analytic model, GALFORM (Cole et al. 2000; Lacey et al. 2016), and the EAGLE simulation project, a state-of-the-art suite of calibrated hydrodynamical simulations (Schaye et al. 2015; Crain et al. 2015).

A number of other authors have presented comparisons of results from hydrodynamical simulations to semi-analytic models, albeit without access to hydrodynamical simulations that predict realistic galaxy properties for representative volumes. Some studies have focused specifically on cooling and gas infall onto galaxies, finding varying levels of agreement (Yoshida et al. 2002; Helly et al. 2003; Monaco et al. 2014). Saro et al. (2010) analysed a single, massive cluster, finding significant differences in the manner with which tidal stripping acts between a semi-analytic model and a hydrodynamical simulation. Stringer et al. (2010) analysed a single disc galaxy, finding it was possible to roughly reproduce a hydrodynamical simulation with an explicitly calibrated semi-analytic model. Cattaneo et al. (2007) and Hirschmann et al. (2012) analysed larger samples of galaxies, both finding broad agreement in stellar and baryonic masses but significant differences when analysed in detail. In particular, Hirschmann et al. (2012) reported large differences in star formation efficiency stemming from local versus global implementations of a Kennicutt star formation law.

This study follows from Guo et al. (2016), who compared GALFORM, the similar L-GALAXIES model (Guo et al. 2011) and EAGLE. They focused on global predictions for the galaxy population (stellar mass functions, star formation rates (SFRs), passive fractions, mass-metallicity relations, mass-size relations). They showed that stellar mass functions and passive fractions were broadly similar between the models (provided gradual ram pressure stripping of hot gas from satellites was implemented in GALFORM). However, they also showed that predictions for galaxy sizes differed significantly and that mass-metallicity relations are significantly steeper in GALFORM than in the reference EAGLE model. In both cases, the predictions from EAGLE are in significantly better agreement with observations.

While these disagreements between the models are highly suggestive of differing baryon cycling (because of discrepant metallicities) and angular momentum evolution (because of discrepant sizes, see also Stevens et al. 2017), from a global comparison it is not clear exactly how these differences arise. Here, we compare the GALFORM and EAGLE models in more detail and attempt to isolate as far as possible distinct physical processes, focussing on those which we expect may not be modelled realistically in semi-analytic models. We also match individual galaxies by matching the haloes between the dark-matter-only version of

EAGLE and the full hydrodynamical simulation. This allows us to assess the difference in stellar mass between individual galaxies.

The results and methodology presented here will, in turn, underpin a future study where we plan to perform the most direct level of comparison possible between GALFORM and EAGLE. Namely, to directly measure all of the mass, metal and angular momentum exchanges between different discrete baryonic reservoirs in EAGLE and compare with the corresponding quantities in GALFORM. As such, we consider here how to compartmentalize baryons in EAGLE between the corresponding discrete components that are tracked in semi-analytic models. In particular, we carefully consider how to separate the interstellar medium (ISM) from more diffuse halo gas in the circumgalactic medium (CGM) in EAGLE on physical grounds.

The layout of this paper is as follows. We introduce the EAGLE simulations, the GALFORM semi-analytic model and describe our analysis methodology in Section 2. We present a first comparison of the models by analysing stellar masses in Section 3. We compare star formation thresholds and efficiencies as well as the angular momentum of star-forming gas in Section 4. We discuss feedback from supernovae (SNe) and active-galactic nuclei (AGN) in Section 6.2 and the resulting baryon cycle in Section 7. We discuss the consequences of qualitative differences between gas infall rates onto galaxies in the two models in Section 8. Finally, we summarise our main results in Section 10.

Throughout this paper we denote the units of distances in proper kiloparsecs as pkpc and comoving kiloparsecs as ckpc. Also throughout, log refers to the base 10 logarithm and ln refers to the natural logarithm.

2 MODELLING GALAXY FORMATION

To facilitate a direct comparison of the EAGLE simulations and the GALFORM model, we follow Guo et al. (2016) by running GALFORM on a dark-matter-only version of the reference EAGLE simulation run with a 100^3 Mpc^3 box (L100N1504 in the convention introduced by Schaye et al. 2015). As described by Guo et al. (2016), both simulations were performed with the same cosmological parameters taken from Planck Collaboration et al. (2014), and with the same initial conditions, following the method of Jenkins (2010).

2.1 EAGLE

The EAGLE simulations are a suite of hydrodynamical simulations of the formation and evolution of galaxies within the context of the Λ CDM cosmological model. Performed using a modified version of the GADGET-3 code (last presented in Springel et al. 2005), they include a state-of-the-art implementation of smoothed particle hydrodynamics (SPH, Dalla Vecchia in prep, Schaller et al. 2015a). They also include a set of subgrid models that account for the physics of photo-heating/ionization from an evolving, uniform background radiation field, radiative cooling from metal lines and atomic processes, star formation, stellar and supermassive black hole evolution and feedback. Subgrid models are included to compensate for the limited resolution of cosmological simulations and the prohibitive computational cost of performing detailed on-the-fly radiative transfer. A detailed overview of these subgrid models can be found in Schaye et al. (2015) and a concise overview tailored to the topic of comparison with semi-analytic models can be found in Guo et al. (2016).

2.2 GALFORM

GALFORM is a continually updated semi-analytic galaxy formation model, first introduced in Cole et al. (2000), which itself was an evolution from earlier models (e.g. Lacey & Cole 1993; Cole et al. 1994). Salient updates subsequent to Cole et al. (2000) include the inclusion of AGN feedback (Bower et al. 2006), the addition of gradual ram-pressure stripping in satellites (Font et al. 2008) and a decomposition of the ISM into neutral atomic and molecular hydrogen components (Lagos et al. 2011). The most recent branches of the model can roughly be divided between a model with a universal stellar IMF (Gonzalez-Perez et al. 2014; Guo et al. 2016), and a model that also implements a non-standard IMF in nuclear starbursts (Lacey et al. 2016).

Guo et al. (2016) introduced a version of the universal IMF model that was explicitly tuned for the EAGLE DM-only simulation using 200 simulation outputs. For this study, we use an updated version of this model which is very similar. The updates were made to ensure that properties of individual galaxies do not depend on random numbers, as discussed below. This is a desirable step for comparing with the EAGLE simulations on an object-by-object basis. Otherwise, the model parameters are the same as Guo et al. (2016), with the exception of slight changes to two parameters which control the efficiencies of SNe and AGN feedback¹. These changes were made to approximately restore predictions for the local stellar mass function presented in Guo et al. (2016) after an error in the calculation of halo concentrations introduced in Guo et al. (2016) was corrected². The calibration of the reference model used here hence follows Guo et al. (2016) and is described in Section 2.7.

To remove a dependency of individual galaxy properties on random numbers, we make two changes with respect to Guo et al. (2016). The first is that we now measure halo spin parameters from the EAGLE dark-matter-only simulation instead of sampling from a probability distribution function, as introduced in Cole et al. (2000). The second is that we now track the orbits of satellites measured in the dark-matter-only simulation. Once satellites can no longer be identified in the simulation, a self-consistent dynamical friction merging timescale, T_{df} , is then computed as

$$T_{df} = \left(\frac{R_c}{R_H}\right)^{1.8} \left(\frac{J}{J_c}\right)^{0.85} \frac{\tau_{dyn}}{2B(1)\ln(\Lambda)} \left(\frac{M_H}{M_S}\right), \quad (1)$$

where R_H is the halo virial radius, R_c is the radius of a circular orbit with the same energy as the actual orbit, J/J_c is the ratio of the angular momentum of the actual orbit to the angular momentum of a circular orbit with the same energy, τ_{dyn} is the halo dynamical time³, M_H is the host halo mass, M_S is the mass of the satellite subhalo, $\ln(\Lambda)$ is the Coulomb logarithm (taken to be $\ln(\Lambda) = \ln(M_H/M_S)$) and $B(x) = \text{erf}(x) - 2x/\sqrt{\pi} \exp(-x^2)$. The full details of this new merging scheme are given in Simha & Cole (2017)⁴.

¹ Specifically, we change the normalisation of the SNe feedback mass loading factor, V_{SN} from 425 km s^{-1} to 380 km s^{-1} and the threshold for AGN feedback, α_{cool} , from 0.52 to 0.8. See Lacey et al. (2016) for the definition of these model parameters.

² Specifically, an incorrect tabulated power spectrum file was used to calculate halo concentrations. This error does not affect any of the conclusions of that study.

³ Defining the halo dynamical time as $\tau_{dyn} = R_H/V_H$, where R_H is the halo virial radius and V_H is the halo circular velocity at the virial radius.

⁴ Note that we do not use the tidal disruption model described in Simha & Cole (2017).

2.3 Structure and assumptions that underpin semi-analytic galaxy formation models

In semi-analytic galaxy formation models such as GALFORM, the initial presupposition is that baryons trace the accretion of dark matter mass and angular momentum onto collapsed dark matter haloes, that the baryons that have been accreted onto dark matter haloes can be compartmentalized into a few discrete components, and that these components can be adequately characterised by a handful of quantities. The hierarchy of galaxy formation is accounted for by including each subhalo as a distinct entity such that the evolution of satellite galaxies is tracked within parent haloes.

The discrete baryonic components typically tracked in a modern semi-analytic galaxy formation model consist of a galaxy disc, a galaxy bulge/spheroid, a diffuse gas halo and a reservoir of gas that has been ejected from the galaxy by feedback. The quantities tracked for each of these components typically include the total mass, the magnitude of the angular momentum, the metal content and a set of scale lengths that specify the spatial distribution, assuming idealised density profiles. These quantities are evolved enforcing mass conservation and (typically) total angular momentum conservation. Galaxy formation is expected to be a highly dissipative process and so energy conservation is not usually explicitly tracked (although see Monaco et al. 2007). However, individual physical processes do often contain energetic considerations, for example in the computation of a radiative cooling timescale for hot diffuse halo gas.

A simplified, linearised version of the mass conservation equations for a central subhalo in GALFORM is

$$\begin{bmatrix} \dot{M}_{diffuse} \\ \dot{M}_{ISM} \\ \dot{M}_{ejected} \\ \dot{M}_\star \end{bmatrix} = \begin{bmatrix} f_B \dot{M}_H \\ 0 \\ 0 \\ 0 \end{bmatrix} + \begin{bmatrix} -\frac{1}{\tau_{infall}} & 0 & \frac{1}{\tau_{ret}} & 0 \\ \frac{1}{\tau_{infall}} & -\frac{(1-R+\beta_{ml})}{\tau_\star} & 0 & 0 \\ 0 & \frac{\beta_{ml}}{\tau_\star} & -\frac{1}{\tau_{ret}} & 0 \\ 0 & 0 & \frac{(1-R)}{\tau_\star} & 0 \end{bmatrix} \begin{bmatrix} M_{diffuse} \\ M_{ISM} \\ M_{ejected} \\ M_\star \end{bmatrix} \quad (2)$$

where $M_{diffuse}$ is the mass in a diffuse gas halo, M_{ISM} is the mass in the interstellar medium, $M_{ejected}$ is the mass in a reservoir of gas ejected from the galaxy by feedback, M_\star is the mass in stars and M_H is the total halo mass. f_B is the cosmic baryon fraction, τ_{infall} is the timescale for halo gas to infall onto a disc, τ_\star is the disc star formation timescale, R is the mass fraction returned from stars to the ISM through stellar mass loss, β_{ml} is the efficiency of SNe feedback⁵ and τ_{ret} is the return timescale for gas ejected by feedback. Alongside Eqn 2, there is also a corresponding set of equations for metal mass and angular momentum. Here, we have neglected the distinction between the disc and bulge/spheroid for simplicity and we have written the star formation law as being linear in the ISM gas mass (which is not the case for GALFORM models following Lagos et al. 2011).

The source term in Eqn 2 is the halo accretion rate, \dot{M}_H , scaled

⁵ Specifically β_{ml} is the mass loading factor, defined as the ratio of the mass outflow rate from galaxies to the star formation rate.

by the cosmic baryon fraction, f_B , to give the baryonic accretion rate. The stellar mass reservoir, M_* , acts as a sink term because stellar recycling is implemented with the instantaneous recycling approximation (Cole et al. 2000). The strongly coupled nature of galaxy formation is encoded in the off-diagonal terms of Eqn 2. Several of these terms (τ_{infall} , τ_* and β_{ml}) depend in a non-linear fashion on different combinations of the halo density profile, halo mass accretion history, halo spin, disc angular momentum and diffuse halo metal content, such that the coupling between various aspects of the model is implicitly tighter than is shown explicitly in Eqn 2.

The terms that appear in the central matrix of Eqn 2 represent distinct physical processes, some of which are analogous to the inclusion of the subgrid models included in EAGLE. These include star formation (τ_*), stellar recycling (R) and the energy injection from stellar feedback (β_{ml}). Other processes are not modelled by subgrid models in EAGLE and emerge naturally within the hydrodynamical simulation (although these will still be affected by uncertain subgrid modelling). These include gas infall from a diffuse halo (characterised by τ_{infall}) and reincorporation from a reservoir of gas ejected from the galaxy by feedback back into the diffuse halo (τ_{ret}).

Additional physical processes included in GALFORM but not shown in Eqn. 2 include metal enrichment of the ISM, the growth of central SMBHs and the resulting AGN feedback, ram-pressure stripping of satellite galaxies, spheroid formation through galaxy mergers and disc instabilities, nuclear starbursts and the suppression of gas accretion onto small haloes by the UV background after reionization (for a complete overview see Lacey et al. 2016).

Table 1 presents a brief summary of the relevant physical processes included in GALFORM and EAGLE, sorted by the order in which they discussed in the following sections. More details for these physical processes are given in Appendix A.

2.4 Subhalo identification & merger trees

In both GALFORM and EAGLE, haloes are identified first as groups using a friends-of-friends (FoF) algorithm, adopting a dimensionless linking length of $b = 0.2$ (Davis et al. 1985). FoF groups are split into subhaloes of bound particles using the SUBFIND algorithm (Springel et al. 2001; Dolag et al. 2009). For EAGLE, galaxies are then defined as the baryonic particles bound to a given subhalo. For each FoF group, the subhalo containing the particle with the lowest value of the gravitational potential is defined as hosting the central galaxy and other subhaloes are defined as hosting satellite galaxies. Galaxy centres are based on the position of the particle with the lowest gravitational potential.

In GALFORM, haloes are identified in the same way using the dark-matter-only version of the reference $L100N1504$ EAGLE simulation. Unlike in EAGLE, groups of subhaloes are then grouped together by the DHALO algorithm presented by Jiang et al. (2014). This algorithm sets the distinction between central and satellite galaxies using information from the progenitors of a given subhalo. In detail, subhaloes are flagged as satellites for the first time when they first enter within twice the half-mass radius of a more massive subhalo and if they have lost at least 25% of their past maximum mass (see Appendix A3 in Jiang et al. 2014). Once a subhalo is identified as a satellite, this status is then preserved for all its descendants for which it is considered the main progenitor. This leads to situations where galaxies are still considered to be satellites even if they have escaped outside the virial radius of a parent host halo and out into the field (see Guo et al. 2016, for a discussion of the

importance of this choice and a comparison with the implementation in the L-GALAXIES model).

We define halo masses in EAGLE (only for central subhaloes) as M_{200} , the total mass enclosed within a radius within which the mean internal density is 200 times the critical density of the Universe. Internally within GALFORM, halo masses are defined simply as the sum of the mass of each subhalo associated with a given DHALO (denoted as M_{DH}). The masses of each subhalo are defined simply as the sum of the particles considered gravitationally bound by SUBFIND to that subhalo. We have also measured M_{200} for central galaxies from the EAGLE dark-matter-only simulation and we use these masses for GALFORM galaxies when comparing galaxy properties at a given halo mass to EAGLE. The differences between these various halo masses are shown in Appendix B. Hereafter, we denote M_H as referring to M_{200} measured from the hydrodynamical simulations for EAGLE galaxies and M_{200} measured from the dark-matter-only simulation for GALFORM galaxies.

As well as the merger trees used in GALFORM, we also construct merger trees for the reference $L100N1504$ EAGLE hydrodynamical simulation using the same subhalo merger tree scheme that underpins the DHALO algorithm. We use these trees only when presenting results that involve tracking the main progenitors of EAGLE galaxies in time. We define the main progenitor as the subhalo progenitor containing the most bound particle. For the merger trees constructed from the hydrodynamical simulation, we ensure in post-processing that the main progenitor is always a dark-matter subhalo, as opposed to a fragmented clump of star and black hole particles.

2.5 Matching haloes

To compare galaxies between EAGLE and GALFORM on an object-by-object basis, we match haloes between the reference EAGLE simulation ($L100N1504$) with the corresponding dark-matter-only simulation, following the methodology of Schaller et al. (2015b). Haloes are matched using unique dark matter particle identifiers (IDs). For each subhalo in the reference EAGLE simulation, the 50 most bound dark matter particles are identified and cross-matched against the particle IDs of subhaloes in the dark-matter-only simulation. If more than half of these particles are found to be associated with a given subhalo in the dark-matter-only simulation, and over half of the corresponding 50 most bound particles from that subhalo belong to the former subhalo (such that the match is bijective), then the match is considered positive. This matching procedure is performed for a selection of redshifts ($z = 0, 2$ & 3.9). The matching statistics are listed in Table 2.

2.6 Compartmentalization

For each baryonic component that is included in GALFORM, we assign baryonic particles to a corresponding component in EAGLE. We first assign baryonic particles to a given subhalo as described in Section 2.4. The baryonic particles associated with a given subhalo and then assigned to one of the following reservoirs:

- Stars-galaxy, M_* - stars associated with the galaxy.
- Stars-ICL, $M_{*,\text{ICL}}$ - stars associated with the intra-cluster medium.
- Halo gas, M_{diffuse} - diffuse circumgalactic halo gas.
- ISM gas, M_{ISM} - gas in the ISM of the galaxy.
- Ejected gas, M_{ejected} - gas that has been ejected (but not later

	GALFORM	EAGLE
Star formation threshold	Disc star formation traces molecular hydrogen. Molecular hydrogen fraction depends on mid-plane gas pressure, which in turn depends on disc gas and stellar mass, and disc size.	Star formation occurs in gas above a local density and metallicity dependent threshold.
Star formation law	Disc star formation rate is linear in molecular gas mass.	Star formation rate scales with local gas pressure, analogous to a Kennicutt-Schmidt law.
Disc angular momentum	Disc angular momentum is calculated assuming infalling gas conserves angular momentum. Gas and stars in the disc have equal specific angular momentum.	Angular momentum is computed locally following gravity and hydrodynamics.
Stellar feedback	Gas is ejected from galaxies (and haloes) as stars are formed, with an efficiency scaling with galaxy circular velocity.	Thermal energy is injected into the ISM around young star particles. The average energy injection scales with local gas density and metallicity. Gas is always heated by $\Delta T = 10^{7.5}$ K.
Black hole growth	SMBHs grow during galaxy mergers and disc instabilities.	SMBHs grow from surrounding ISM with an Eddington-limited Bondi accretion rate.
AGN feedback	SMBHs truncate gas infall onto the disc if the surrounding halo is quasi-hydrostatic and the SMBH injects enough energy to offset the radiative cooling rate.	Accreting SMBHs inject thermal energy into the surrounding ISM with a fixed average efficiency. Gas is always heated by $\Delta T = 10^{8.5}$ K.
Gas return	Gas ejected from haloes by stellar feedback returns to the halo over a halo dynamical time.	Gas return depends on particle trajectories which follow gravity and hydrodynamics. These trajectories are (presumably) sensitive to stellar and AGN feedback parameters, including the heating temperature.
Gas infall	Gas infall onto galaxy discs is either limited by gravitational freefall or radiative cooling timescales, depending on halo gas and dark matter density profiles, halo gas metallicity, and the time elapsed since halo mass-doubling events.	Gas infall is computed locally following gravity and hydrodynamics.

Table 1. Summary of the modelling of physical processes which are relevant to the results presented in this study, sorted by the order in which these processes are discussed.

$\log(M_*/M_\odot)$		8 – 9	9 – 10	10 – 11	11 – 12
$z=0.0$	f_{tot}	0.79	0.91	0.96	0.96
	f_c	0.97	0.99	0.99	0.98
	f_s	0.55	0.81	0.91	0.88
$z=2.0$	f_{tot}	0.84	0.95	0.95	1
	f_c	0.98	0.98	0.96	1
	f_s	0.57	0.87	0.91	1
$z=3.85$	f_{tot}	0.91	0.97	0.95	-
	f_c	0.97	0.98	0.95	-
	f_s	0.66	0.91	0.85	-

Table 2. Statistics for successful matches between haloes in the dark-matter-only and reference EAGLE simulation. Binning galaxies by stellar mass in EAGLE, the fractions of successful matches for central, satellite and all galaxies (f_c , f_s and f_{tot} respectively) are presented for three different redshifts. Note that at $z = 3.85$, there are no galaxies with $M_* > 10^{11} M_\odot$. Here, we use EAGLE rather than GALFORM to define whether matched galaxies are considered centrals or satellites.

reincorporated) from the subhalo. Note that this reservoir therefore (only) includes particles that are not bound to the subhalo.

The galactic stellar component is straightforwardly defined as the stellar particles within 30 pkpc of the subhalo centre, following Schaye et al. (2015). This aperture is used to make a distinction between stars in the galaxy and the significant, extended intracluster light component that exists around massive, $M_* \sim 10^{11} M_\odot$ galaxies in EAGLE. We do not include such an aperture for GAL-

FORM galaxies at present because the corresponding massive galaxies have much smaller half-light radii than in EAGLE (Guo et al. 2016). When analysing results from EAGLE, we do not attempt to distinguish between stellar disc and spheroid components. Unless otherwise stated, all stellar properties presented from GALFORM are computed by summing bulge and disc components.

In GALFORM, the ISM consists of two components: a rotationally supported gas disc and a nuclear component that is associated with bursts of star formation. The remaining gas within a given subhalo is then grouped together as a circumgalactic halo-gas component. We define a corresponding ISM component in EAGLE by selecting gas particles within a given subhalo that are either rotationally supported against collapse to the halo centre or are spatially coincident with the galactic stellar component.

We select rotationally supported gas particles as those that satisfy both

$$-0.2 < \log_{10} \left(\frac{2\epsilon_{k,\text{rot}}}{\epsilon_{\text{grav}}} \right) < 0.2, \quad (3)$$

and

$$\frac{\epsilon_{k,\text{rot}}}{\epsilon_{k,\text{rad}} + \epsilon_{\text{th}}} > 2, \quad (4)$$

where $\epsilon_{k,\text{rot}}$ is the rotational specific kinetic energy associated with

motion orthogonal to the radial vector orientated from the gas particle to the subhalo centre⁶. $\epsilon_{k,\text{rad}}$ is the corresponding specific kinetic energy associated with radial motion. ϵ_{grav} is the specific gravitational energy defined as $GM(r)/r$ and ϵ_{th} is the specific internal energy.

Eqn 3 acts to select gas particles that have the correct rotational kinetic energy to be in rotational equilibrium against the gravitational potential at a given radius. Eqn 4 acts to remove particles with significant radial motion or with significant thermal energy. Put together, Eqns 3 and 4 act to separate the rotationally supported ISM from a diffuse, hot gaseous halo or from radially infalling accretion streams.

In addition to rotationally supported gas, we also select gas particles that are spatially coincident with the stellar galactic component. Specifically, we select any dense gas ($n_{\text{H}} > 0.03 \text{ cm}^{-3}$) that is within twice the half-mass radius, $r_{1/2,*}$ of the stellar component of the subhalo. This acts to select dense, nuclear ISM gas that is typically pressure supported because of the imposed ISM equation of state in EAGLE (Schaye et al. 2015).

Finally, we apply a number of radial cuts that act to remove distant, rotationally supported material that is clearly not spatially coincident with the ISM. For inert, passive galaxies with no centrally peaked ISM component, additional care must be taken to use radial cuts appropriate for these systems.

Specifically, we assign gas particles to the ISM in EAGLE by applying the following selection criteria in the following order:

- (i) We require that ISM gas must be cooler than 10^5 K or be denser than 500 hydrogen nuclei per cubic centimeter.
- (ii) We require that the ISM must be rotationally supported (Eqns 3 and 4) or be dense ($n_{\text{H}} > 0.03 \text{ cm}^{-3}$) and within $2r_{1/2,*}$.
- (iii) We remove ISM gas that is beyond half the halo virial radius (this step is only applied for central galaxies).
- (iv) We remove remaining ISM gas that is beyond $2r_{90,\text{ISM}}$ (non-iteratively). The radius enclosing 90% of the ISM mass, $r_{90,\text{ISM}}$, is calculated after the previous selection criteria have already been applied.
- (v) If the galaxy has a remaining ISM gas ratio of $M_{\text{ISM}}/M_* < 0.1$, we apply a passive-galaxy correction and remove ISM gas beyond $5r_{1/2,*}$.

A more detailed justification and discussion of these ISM definitions is given in Appendix C, along with a number of examples. Importantly, we find that the resulting ISM mass can be significantly different compared to if the ISM is instead defined simply as star-forming gas (see also Section 4.1). We also show that the ISM definition used here is similar at low redshifts to selecting mass in neutral hydrogen within a 30 pkpc aperture, as used in Lagos et al. (2015). However, at higher redshifts ($z > 2$), increasingly large fractions of hydrogen in the radially infalling CGM are in a neutral phase. As such, the ISM definition used here starts to diverge from taking neutral gas within an aperture.

Appendix C also demonstrates the important point that a simple decomposition of baryons within haloes into distinct components does not always provide a good description of the complex nature of what truly occurs in simulations and in reality. The separation between the CGM and a rotation/pressure/dispersion supported ISM can be a well posed question for many galaxies, par-

ticularly at low redshift. For some galaxies however, the distinction becomes much less clear. Appendix C shows an example of a massive, high-redshift star forming galaxy with dense, star-forming gas distributed over a significant fraction of the halo virial radius. For such galaxies, the assumption that there is a centrally concentrated ISM which is in dynamical equilibrium clearly starts to break down.

With gas particles belong to the ISM selected, we assign the remaining (non-ISM) gas particles associated with a given subhalo to a diffuse halo-gas component. Finally, we also define a reservoir of gas that has been ejected beyond the virial radius by feedback. Note that gas that has been previously ejected but has since been reincorporated back inside the halo virial radius is not counted in this ejected gas reservoir. In GALFORM, this reservoir is explicitly tracked. For EAGLE, we estimate the mass in this reservoir, M_{ejected} , by taking the difference

$$M_{\text{ejected}} = f_{\text{B}} M_{\text{H}} - M_{\text{B}} \quad (5)$$

where f_{B} is the cosmic baryon fraction and M_{B} is the total baryonic mass (including satellite subhaloes) within R_{200} . Under this approximation, gas that was prevented from ever being accreted onto the halo in EAGLE is also included in the ejected gas reservoir (assuming the halo would otherwise accrete gas at the cosmological baryon fraction). In future work, we plan to more accurately compute the properties of this reservoir by tracking the past/future trajectories of gas particles accreted onto haloes.

2.7 Model calibration

Both GALFORM and the EAGLE simulations contain a number of model parameters that can be adjusted to reproduce observational constraints. The resulting calibration process is typically performed by hand without any statistically rigorous exploration of the model parameter space, although this machinery has been developed and applied for semi-analytic models in recent years (e.g. Henriques et al. 2013; Benson 2014; Lu et al. 2014; Rodrigues et al. 2017). This calibration approach is necessary primarily because it is not possible at present to simulate the resolved physics of star formation and feedback or to model the resulting effects from first principles. The observational constraints on model parameters range from direct constraints like the observed Kennicutt-Schmidt star formation law to indirect constraints such as the luminosity function of galaxies. Broadly speaking, parameters relating to star formation can be calibrated directly (Schaye 2004; Schaye & Dalla Vecchia 2008; Lagos et al. 2011) while parameters relating to stellar feedback, SMBH accretion and AGN feedback are calibrated using indirect constraints. For the scientific work performed using GALFORM and EAGLE, the underlying philosophy regarding calibration is that a minimal set of observations are used to adequately constrain the model parameter spaces, and that following calibration the models can be compared to other observables with some degree of predictive power (Cole et al. 2000; Schaye et al. 2015).

Calibration of the model parameters in the EAGLE simulations is described in Schaye et al. (2015) and Crain et al. (2015). Calibration of the model parameters for the GALFORM model used here follows Guo et al. (2016). Briefly, GALFORM was calibrated to match the observed local luminosity functions in the b_J and K bands from Norberg et al. (2002) and Driver et al. (2012), as well as the SMBH-bulge mass relation from Häring & Rix (2004). EAGLE was calibrated to match the local stellar mass functions inferred from observations by Li & White (2009) and Baldry et al.

⁶ Note that there is therefore no preferred rotation direction in our ISM selection criteria and no distinction is made between gas particles that are corotating and those that are counter-rotating with respect to the ensemble.

(2012), the local stellar mass-size relation from Shen et al. (2003) and Baldry et al. (2012) and the SMBH mass versus total stellar mass relation from McConnell & Ma (2013)⁷.

While EAGLE and GALFORM were calibrated using different observational datasets, Trayford et al. (2015) have demonstrated that EAGLE agrees well with observed u and K -band luminosity functions. The GALFORM model used here predicts a similar stellar mass function to EAGLE at $z = 0$, albeit with a slight deficit of galaxies around the knee. Galaxy sizes at $z = 0$ in GALFORM do not agree with observations (see Appendix D). Black hole masses are comparable between EAGLE and GALFORM at $z = 0$ (see Appendix E).

3 COMPARING STELLAR MASSES

A zeroth order comparison between the reference GALFORM model used here and the reference EAGLE simulation is shown in Fig. 1, which shows the distribution of stellar mass at a given halo mass for central galaxies. By construction, the two models are in approximate agreement at $z = 0$ where both models have been calibrated to similar constraints. The models then diverge at $z = 2, 3.85$, such that GALFORM has a steeper relation between stellar mass and halo mass.

Compared to EAGLE, GALFORM has a significantly larger scatter in stellar mass at a halo mass $\sim 10^{12} M_{\odot}$. For EAGLE, Matthee et al. (2017) showed that 0.04 dex of the scatter is connected to halo concentrations (or equivalently halo assembly times), with the remaining scatter being uncorrelated to any of the (dark matter only) halo properties they explored. In appendix B of Mitchell et al. (2016), we showed that the enhanced scatter at this halo mass range in GALFORM is caused by the differing efficiency of SNe feedback (and hence the efficiency of stellar mass assembly in a holistic sense) between quiescent star formation in discs and triggered nuclear star formation associated with galaxy mergers and disc instabilities (see also the discussion in Guo et al. 2016). This differing efficiency is caused by scaling the efficiency of SNe feedback with disc circular velocity for disc star formation and scaling with bulge circular velocity for SNe feedback associated with triggered nuclear star formation. This in turn leads to a bimodal distribution in stellar mass at a given halo mass in the mass range for which the contributions to the total stellar mass from stars formed in discs and stars formed in nuclear bursts are comparable⁸.

Fig. 2 compares the stellar masses of matched individual galaxies from the two reference models. At $z = 0$, the medians of the distribution are approximately consistent with a unity ratio between the two models. This primarily reflects the fact that both models are calibrated by luminosity/stellar mass function data from the local Universe. Of more interest is the scatter in the distribution. Taking the average over stellar mass bins for $M_{\star} > 10^8 M_{\odot}$, the mean 1σ scatter in the logarithmic distribution is $\sigma = 0.37$ dex.

⁷ EAGLE was compared to the latter data set using the AGN feedback parameter value from the OWLS model. The fit was deemed satisfactory, so no calibration was necessary. However, Booth & Schaye (2009, 2010) have shown that the black hole masses are determined by the subgrid AGN feedback efficiency.

⁸ The mass range for which this occurs is set by AGN feedback in the sense that it acts to prevent late-time disc star formation from overwhelming the contribution from nuclear star formation which tends to dominate in massive galaxies at high redshift (Lacey et al. 2016).

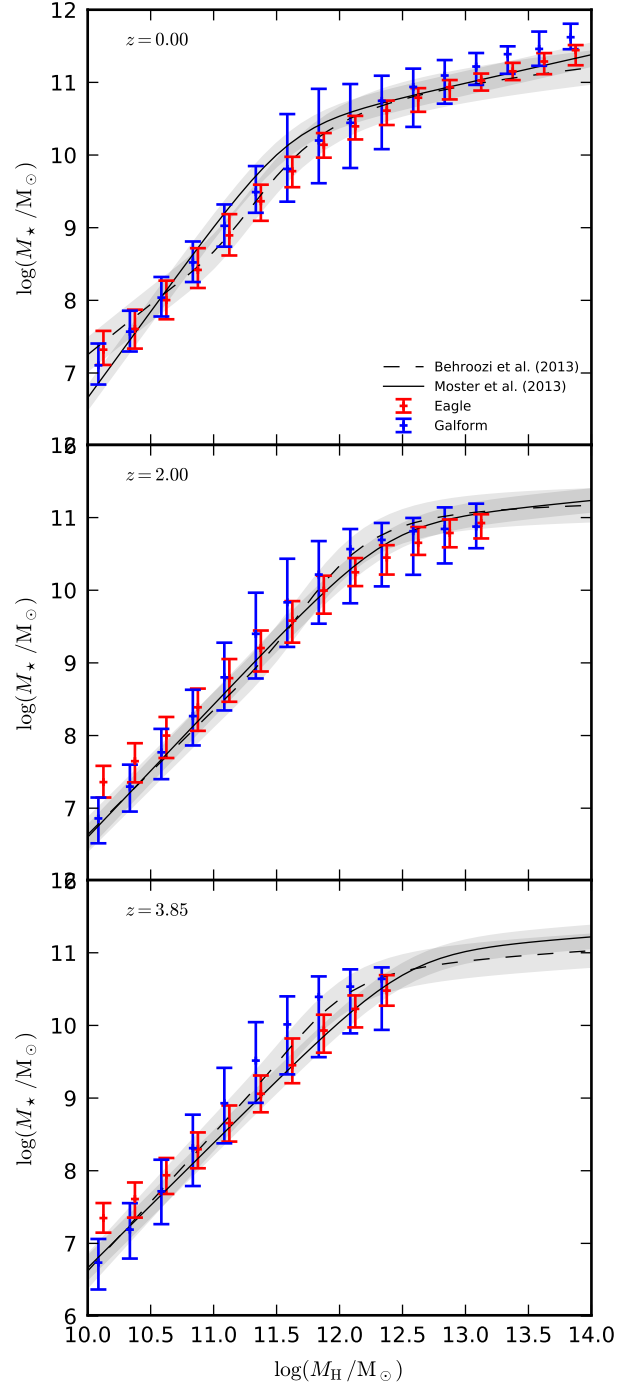


Figure 1. Distribution of stellar mass as a function of halo mass for central galaxies. Each panel corresponds to a different redshift, as labelled. Blue points show the 16, 50 and 84th percentiles for the reference GALFORM model. Red points show the corresponding information for the reference EAGLE simulation. Abundance matching results from Behroozi et al. (2013) and Moster et al. (2013) are shown as dashed and solid black lines. The shaded regions show the assumed/best-fit intrinsic scatter in the distribution.

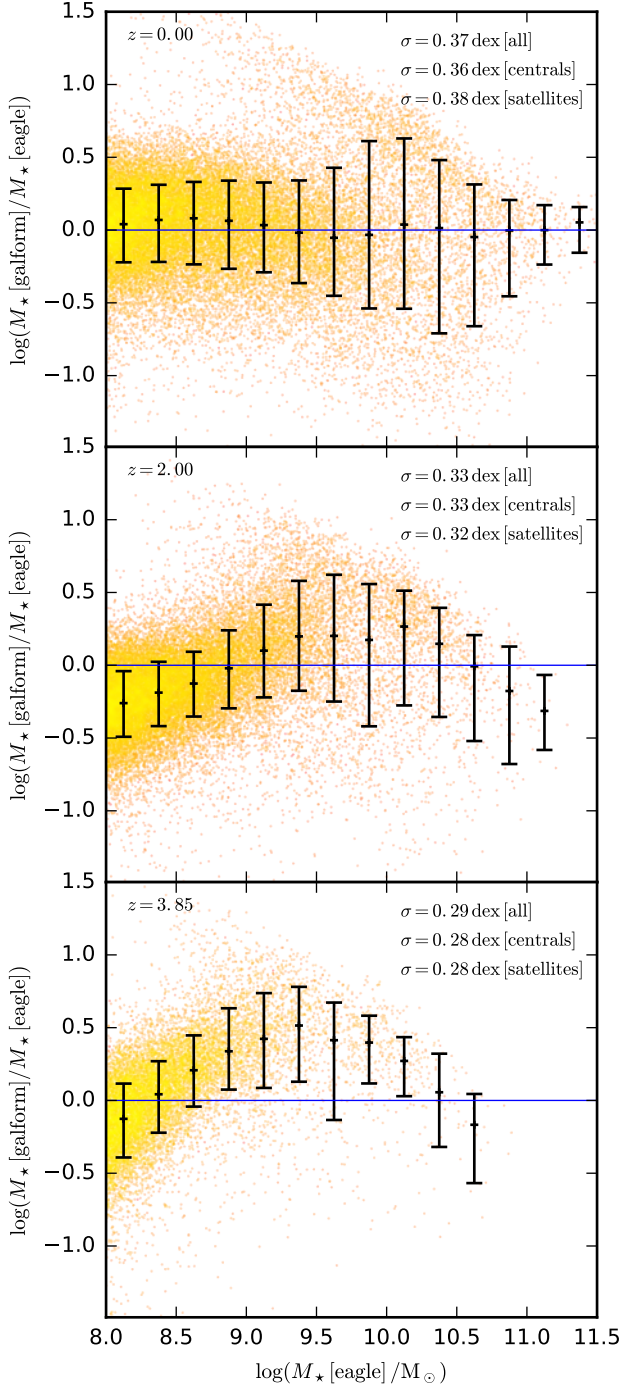


Figure 2. Ratio of the stellar mass in GALFORM to the stellar mass in EAGLE plotted as a function of stellar mass in EAGLE. Each panel corresponds to a different redshift, as labelled. Points and error bars show the 16, 50 and 84th percentiles of the distribution. σ quantifies the 68% range scatter for all, central and satellite galaxies, computed by taking the mean of the scatter for bins over the stellar mass range, $M_* > 10^8 M_\odot$.

As such, GALFORM typically yields the same stellar masses as EAGLE galaxies to within a factor 2.3 at $z = 0$. This significantly exceeds the scatter in halo mass between matched haloes from the EAGLE hydrodynamical and dark-matter-only simulations (0.04 dex at $z = 0$, see Appendix B). It is notable that the level of scatter is elevated for $10 < \log(M_*/M_\odot) < 10.5$. This reflects the increased scatter in stellar mass at a given halo mass seen in Fig. 1 for this mass range.

At $z = 2$ and $z = 4$, the medians of the distribution are no longer consistent with a ratio of unity, reflecting the different shapes of the $M_* - M_H$ distributions predicted by the two models at these redshifts (see Fig. 1). The scatter around the median drops with increasing redshift, indicating that the stellar masses of individual galaxies gradually diverge between the models as the galaxies evolve. Decomposing the scatter between central and satellite galaxies shows that satellites are equivalent to central galaxies in the level of agreement between the models. We explore the underlying reasons for the overall level of scatter seen in Fig. 2 in Section 8.1, where we show that the implementation of gas infall and AGN feedback in GALFORM leads to artificially oscillating baryonic assembly histories for individual galaxies.

4 STAR FORMATION AND THE ISM

4.1 Star formation threshold

In EAGLE, a local metallicity-dependent density threshold is used to decide which gas particles are star-forming (Schaye et al. 2015). In GALFORM, star formation occurs in molecular gas, and the formation of a molecular phase is explicitly computed following empirical correlations inferred from observations (Lagos et al. 2011). Further details of the modelling are presented in Appendix A1.

Fig. 3 shows the mass fraction of ISM gas that is actively forming stars. In both reference models, this distribution evolves with redshift, reflecting the evolution of galaxy disc surface density profiles, the incidence of disc instabilities and galaxy mergers in GALFORM, and the evolution in local ISM density and metallicity in EAGLE. At $z = 0$, the two models display qualitatively different behaviour. While both models predict high star-forming ISM fractions for massive galaxies (where overall gas fractions are very low), GALFORM predicts significantly lower star-forming fractions in low-mass galaxies.

In the reference EAGLE simulation, the gas-phase mass-metallicity relation is shallow at $z = 0$, in tension with observational constraints which imply a lower gas metallicity in low-mass galaxies (See figure 13 in Schaye et al. 2015). As such, we expect that were EAGLE to predict more realistic metallicities for low-mass galaxies, the star-forming ISM fraction would be correspondingly lower. We can test this hypothesis by considering the higher resolution recalibrated EAGLE model (magenta lines in Fig. 3). In this model, the mass-metallicity relation is steeper, in better agreement with observations (Schaye et al. 2015). Correspondingly, Fig. 3 shows that the star-forming ISM fraction is smaller for this model in low-mass galaxies.

While GALFORM does not reproduce the observed metallicities either (see Guo et al. 2016), this is irrelevant for star formation because the star formation threshold has no metallicity dependence in this model. Unlike EAGLE, however, GALFORM predicts galaxy sizes for low-mass late-type (disc) galaxies that are too large compared to observations in GALFORM (the galaxy size distributions as a function of stellar mass are shown in Appendix D). As

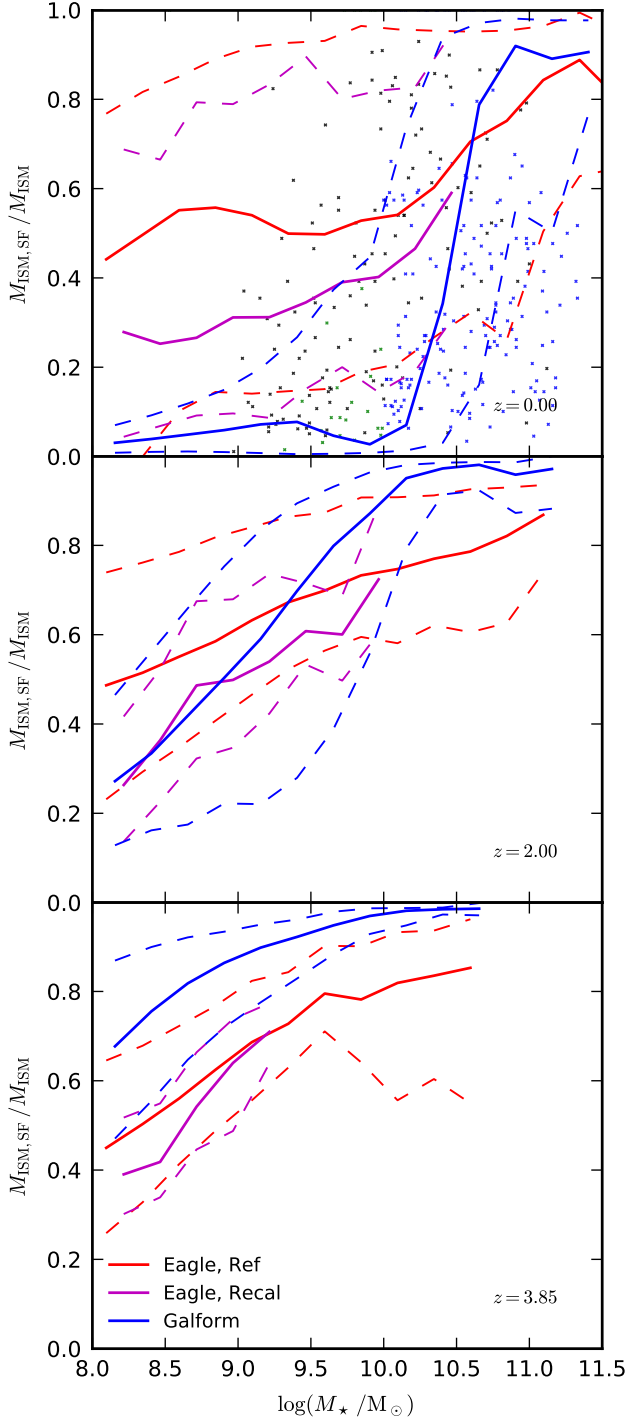


Figure 3. Mass fraction of hydrogen in the ISM that is star-forming as a function of stellar mass. Red and blue lines show the distributions from EAGLE and GALFORM respectively. Magenta lines show the distribution from the higher resolution, recalibrated EAGLE model. Solid lines show the medians and dashed lines show the 16 and 84th percentiles of the distributions. Small grey, green and blue points show respectively observational data from the HRS, ALLSMOG, GASS plus COLD GASS surveys (Catinella et al. 2010; Saintonge et al. 2011; Boselli et al. 2014; Bothwell et al. 2014). Each panel corresponds to a different redshift, as labelled.

such, gas surface densities (for a given ISM mass) will be unrealistically low in low-mass galaxies, potentially leading to unrealistically low molecular gas fractions. Observational data from the Herschel Reference Survey (HRS, Boselli et al. 2014), the APEX low-redshift legacy survey for molecular gas (ALLSMOG, Bothwell et al. 2014), the Galex Aricebo SDSS survey (GASS, Catinella et al. 2010) and the CO legacy database for GASS (COLD GASS, Saintonge et al. 2011) indicate that is indeed the case, with a significant number of detected galaxies with higher molecular-to-atomic gas fractions than is predicted by GALFORM for stellar masses lower than $10^{10} M_{\odot}$. The data also indicates that there are massive galaxies with lower molecular-to-total ISM gas fractions than those predicted by either GALFORM or EAGLE (taking molecular-to-total ratio as a proxy for the star-forming to total ISM ratios shown for EAGLE).

At higher redshifts, Fig. 3 shows that the fraction of mass in the star-forming ISM in the two reference models comes into slightly better agreement. Qualitative differences remain however. At $z = 2$, GALFORM exhibits a steeper trend with stellar mass. At $z = 3.85$, the star-forming ISM fraction is systematically higher by 20% in GALFORM at all stellar masses.

4.2 Star formation law

In EAGLE, star-forming gas is turned into stars following a Kennicutt-Schmidt star formation law, reformulated as a pressure law (Schaye & Dalla Vecchia 2008; Schaye et al. 2015). In GALFORM, the star formation rate in galaxy discs is linear in the molecular gas mass in the disc, with a constant, empirically constrained conversion efficiency (Lagos et al. 2011). Further details of this modelling are presented in Appendix A2.

Fig. 4 shows the SFR per unit star-forming ISM mass for actively star-forming galaxies (which we define as specific SFR $> 0.01, 0.1, 0.1 \text{ Gyr}^{-1}$ for $z = 0, 2, 3.85$ respectively⁹). At $z = 0$, GALFORM has a slightly higher star formation efficiency but agrees with EAGLE (for both the reference and recalibrated simulations) to within $\approx 40\%$, except for the most massive galaxies in the simulation. At higher redshifts, the agreement worsens as EAGLE displays a significant positive trend of efficiency with stellar mass. Star formation efficiency also increases with redshift at fixed stellar mass in EAGLE (albeit more strongly for more massive galaxies). This reflects the changing ISM conditions for the star-forming gas in EAGLE with mass/redshift. At high-redshift, the typical densities of star-forming ISM gas increase in the simulation, accordingly increasing the gas pressure and hence the efficiency of star formation, following Eqn A3 (see figure 12 from Lagos et al. 2015). Despite assuming that star formation in galaxy discs has a fixed efficiency for star-forming gas, this effect is somewhat accounted for in GALFORM by the inclusion of explicit nuclear bursts of star formation. This elevates the net star formation efficiency of a subset of the massive galaxies at high-redshift, albeit with a very skewed distribution compared to EAGLE.

4.3 Gas fractions

The result of the differing star formation thresholds and efficiencies (as well as the effect of accretion and outflow rates, which we do not

⁹ This is guided by the distributions of specific SFR for GALFORM and EAGLE shown in figure 1 of Mitchell et al. (2014) and figure 7 from Guo et al. (2016)

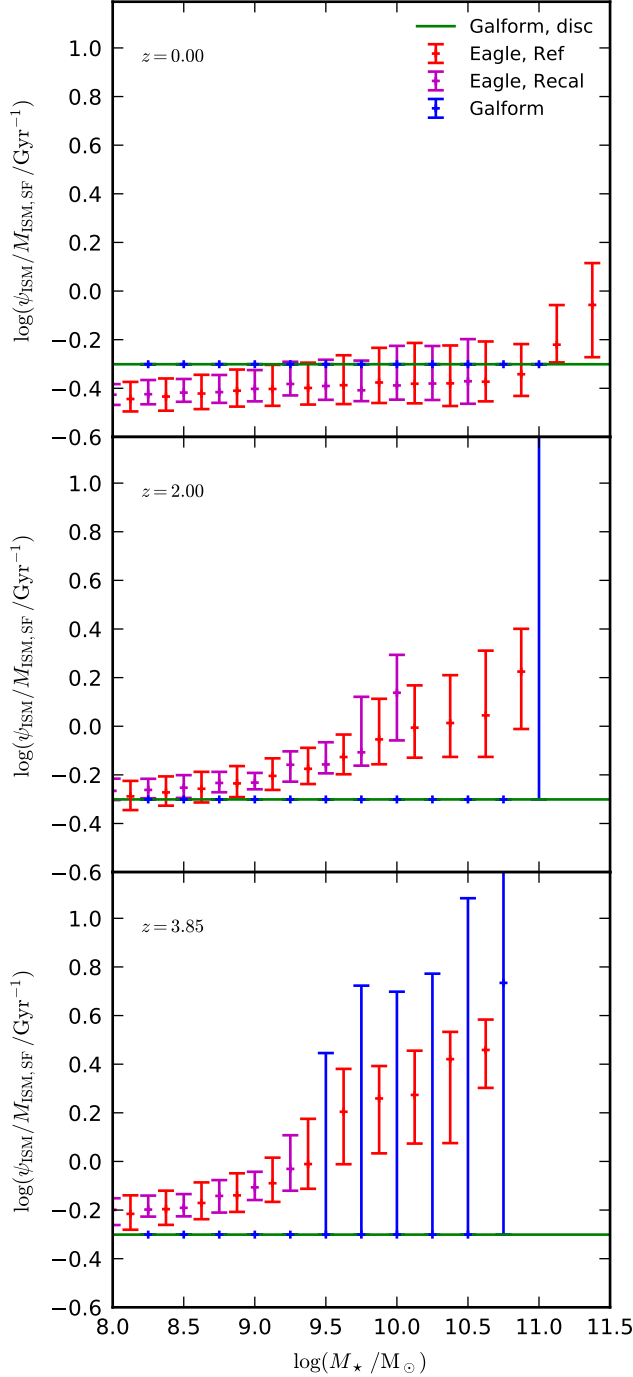


Figure 4. SFR per unit star-forming ISM mass, plotted as a function of stellar mass for actively star-forming galaxies (see text for details). Red and blue points show respectively the distributions from the reference EAGLE and GALFORM models. Magenta points show the distribution from the higher resolution, recalibrated EAGLE simulation. Also shown is the SFR per unit star-forming ISM mass that occurs in galaxy discs in GALFORM (by construction a constant, indicated by green lines), which excludes the contribution from disc-instability or merger triggered starbursts. Points and error bars show the 16, 50 and 84th percentiles of the distributions. Each panel corresponds to a different redshift, as labelled.

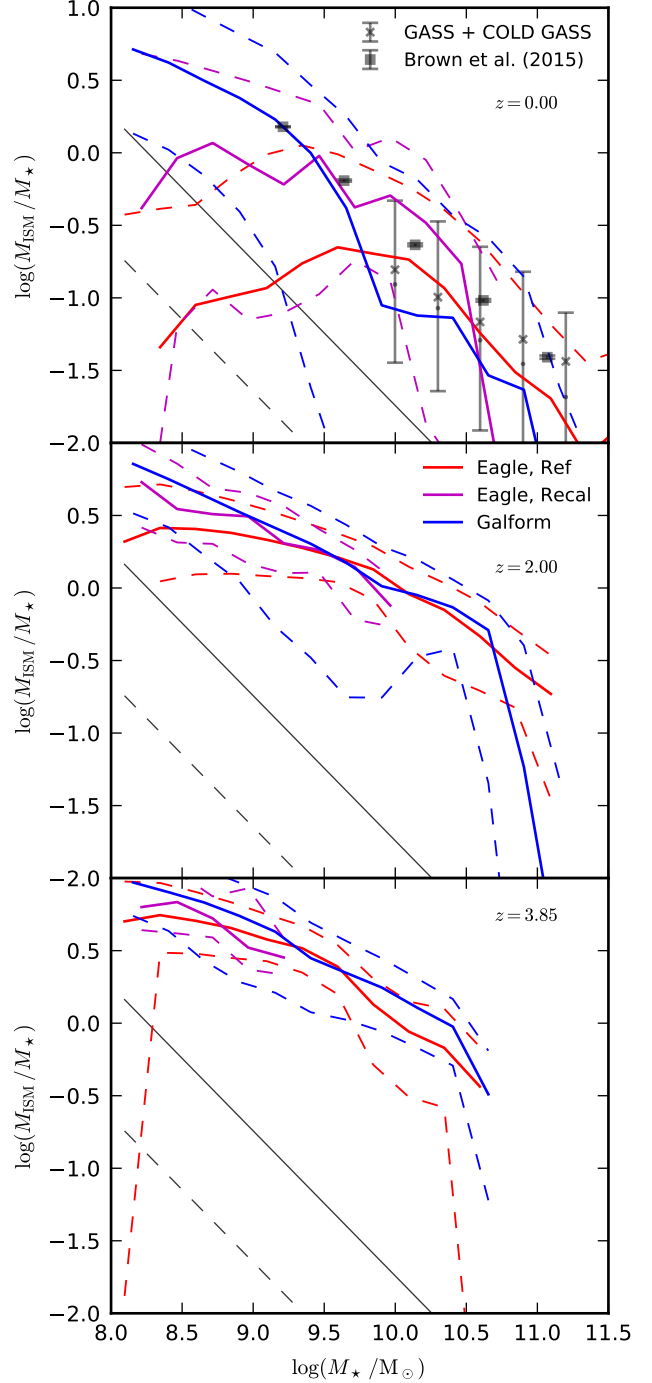


Figure 5. ISM gas ratios as a function of stellar mass. Red and blue lines show the distributions from the reference EAGLE and GALFORM models respectively. Magenta lines show the distribution from the higher resolution, recalibrated EAGLE model. Solid lines show the medians and dashed lines show the 16 and 84th percentiles of the distributions. Solid grey lines mark the point below which the number of gas particles in the ISM drops below 100 in the reference EAGLE simulation. The dashed grey lines mark the corresponding point for the higher resolution, recalibrated EAGLE simulation. Black points show gas ratios of neutral gas from the GASS and COLD GASS surveys and atomic gas ratios from Brown et al. (2015). For GASS/COLD GASS, the error bars indicate the 1 sigma intrinsic scatter of the distribution. Each panel corresponds to a different redshift, as labelled.

measure here) are reflected in the galaxy gas-to-stellar mass ratios (M_{ISM}/M_*), shown in Fig. 5. For galaxies with $M_* > 10^{10} M_\odot$ at $z = 0$, the two models are consistent with each other and with the GASS and COLD GASS surveys. At lower masses, the gas ratios in the reference EAGLE simulation drop until there are typically only a handful of gas particles in the ISM of a galaxy of $M_* \sim 10^8 M_\odot$. In stark contrast, GALFORM predicts that low-mass galaxies have much higher gas ratios, such that the gas ratio decreases monotonically with increasing stellar mass. The median gas ratios in GALFORM are consistent with the stacked atomic gas ratios from Brown et al. (2015) (note that in this regime, the ISM is almost entirely atomic in GALFORM, see Fig. 3).

At higher redshifts, the two models are in better agreement, both showing the expected trend of increasing gas ratio with redshift (although there is little difference $z = 2$ and $z = 4$). Here, it appears that a higher star formation efficiency in EAGLE (Fig. 4) is compensated for by a lower fraction of the ISM which is forming stars (Fig. 3). We have confirmed that EAGLE and GALFORM are indeed very similar at these redshifts in the star formation efficiency per unit total ISM mass (as opposed to the efficiency per unit star-forming ISM mass shown in Fig. 4).

Fig. 5 also shows the gas ratios from the higher-resolution, recalibrated EAGLE model. This indicates that the non-monotonic behaviour seen for the reference EAGLE model at $z = 0$ is likely a resolution effect. The recalibrated model shows similar non-monotonic behaviour but at a lower stellar mass. The recalibrated model is in better agreement with GALFORM and the observational data as a result. Grey solid and dashed lines show the point below which the number of gas particles in the ISM drops below 100 for the reference and recalibrated EAGLE models respectively. This indicates that resolution is indeed likely to be an issue for galaxies with $M_* < 10^{10} M_\odot$ in the reference EAGLE model at $z = 0$ (see the discussion in Crain et al. 2017) and may also affect the higher-resolution recalibrated model for $M_* < 10^9 M_\odot$.

To summarise the differences between GALFORM and EAGLE seen in this section (Fig. 3, 4 and 5), we have demonstrated that gas-to-stellar mass ratios are much higher in GALFORM than in EAGLE for low-mass galaxies at $z = 0$ (with an apparent connection to numerical resolution in EAGLE), but that the models are in good agreement at higher redshifts. For low-mass galaxies at low-redshift, this difference seems to be connected to the difference in the fraction of the ISM that is star-forming (with GALFORM having much lower star-forming ISM fractions). A simple explanation for this difference in star-forming ISM fraction is that because low-mass galaxy sizes are significantly larger in GALFORM than in EAGLE at $z = 0$ (see Appendix D), leading to lower gas surface densities at a given gas fraction and stellar mass in GALFORM. At higher redshifts, the star-forming ISM fractions are less discrepant but EAGLE has a significantly higher median star-formation efficiency than GALFORM for the star-forming ISM in massive galaxies. This translates to very similar gas-to-stellar mass ratios with respect to GALFORM, partly because the differences in star-forming ISM fraction and star formation efficiency compensate for each other, and possibly because the burst mode of star-formation in GALFORM does indeed compensate for the increased median efficiency in EAGLE.

5 ANGULAR MOMENTUM

An important difference between EAGLE and GALFORM concerns the angular momentum of newly-formed stars (for full details of

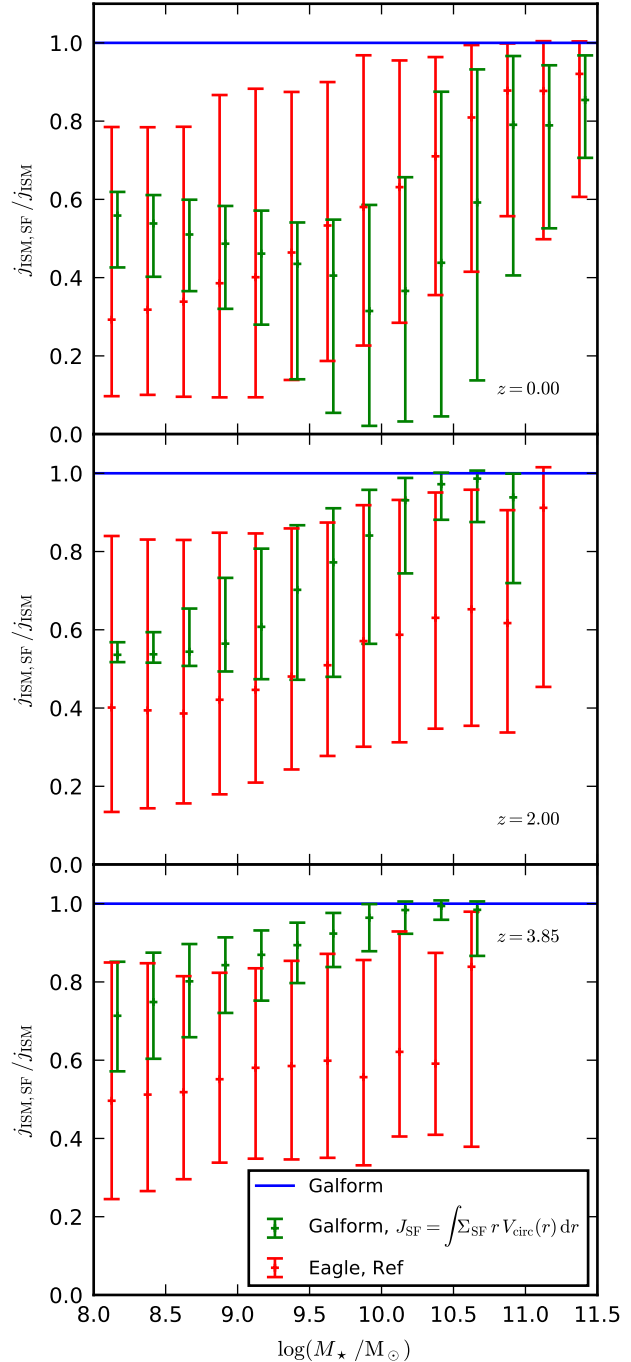


Figure 6. Ratio of specific angular momenta of the star-forming ISM, $j_{\text{ISM,SF}}$ to that of the total ISM, j_{ISM} . Red points show the distribution from EAGLE. The blue line shows the unity ratio implicitly assumed in GALFORM. Green points show the distribution GALFORM would predict were the star-forming disc gas to have angular momentum self-consistent with the radial profile of molecular hydrogen, assuming a flat rotation curve. Here, we make the approximation that nuclear ISM gas undergoing bursts of star formation has no angular momentum. Points and errorbars show the 16, 50 and 84th percentiles of the distributions. Each panel corresponds to a different redshift, as labelled.

angular momentum modelling in GALFORM, see Appendix A3). In EAGLE, stellar particles self-consistently inherit the angular momentum of the gas from which they formed. Historically, this was also the case in older GALFORM models when there was no partition between atomic and molecular gas (and hence no star formation threshold) (Cole et al. 2000). Specifically, it was assumed that the gas and stars within the disc shared a common radial scale length and correspondingly had identical specific-angular momentum. While a simplifying assumption, this did ensure that newly-formed stars had consistent specific angular momentum with the star-forming gas. After the introduction of a radius-dependent partition between atomic and molecular hydrogen by Lagos et al. (2011) this assumption was retained. As such, newly-formed stars in our reference GALFORM model have the same specific angular momentum as the total ISM gas disc, rather than just that of the star-forming ISM (molecular hydrogen). Given that the star-forming, molecular ISM is more centrally concentrated than the atomic ISM under the Lagos et al. (2011) scheme, this means that newly-formed stars have inconsistently high specific angular momentum in GALFORM.

This is explicitly demonstrated in Fig. 6, where we show the ratio of (magnitude of the) specific angular momentum in the star-forming ISM to specific angular momentum in the total ISM. Compared to the unity ratio implicitly assumed in GALFORM, EAGLE predicts that stars form preferentially out of ISM with lower specific angular momentum. In other words, star formation is centrally concentrated in EAGLE. This can be understood as a consequence of the (metallicity-dependent) density threshold implemented in EAGLE. (ISM gas is more likely to pass the threshold at the galaxy centre where densities are highest). There is significant scatter in the distribution, presumably reflecting the vector nature of angular momentum (which is ignored in GALFORM) being affected by complexity of merger events and accretion flows changing in orientation over time (Lagos et al. 2017a,b).

The green points in Fig. 6 show the ratio of specific angular momenta that GALFORM would predict were it to self-consistently compute the angular momentum content of star-forming gas from the radial profile of molecular hydrogen¹⁰. Given that it is otherwise not defined in the model, we have assumed here that star-forming nuclear gas present in galaxy bulges has zero (net) angular momentum, although in practice this choice has negligible effect on the distributions shown. From Fig. 6, it is apparent that were GALFORM to self-consistently compute the angular momentum of the star-forming ISM when computing the angular momentum of newly-formed stars, then EAGLE and GALFORM would come into better agreement on average.

The impact of the assumptions regarding specific angular momentum of newly-formed stars is made clear in Fig. 7. Focussing first on EAGLE, the red and magenta lines show respectively the specific angular momenta of stars and the total ISM in EAGLE. These distributions are separated by almost an order of magnitude in specific angular momentum at a given stellar mass. The actively star-forming ISM in EAGLE (green lines) has intermediate specific angular momentum between the total ISM and stars.

At intermediate stellar masses ($M_\star \sim 10^{10} M_\odot$) at $z = 0$, the ISM in EAGLE has the same specific angular momentum as the

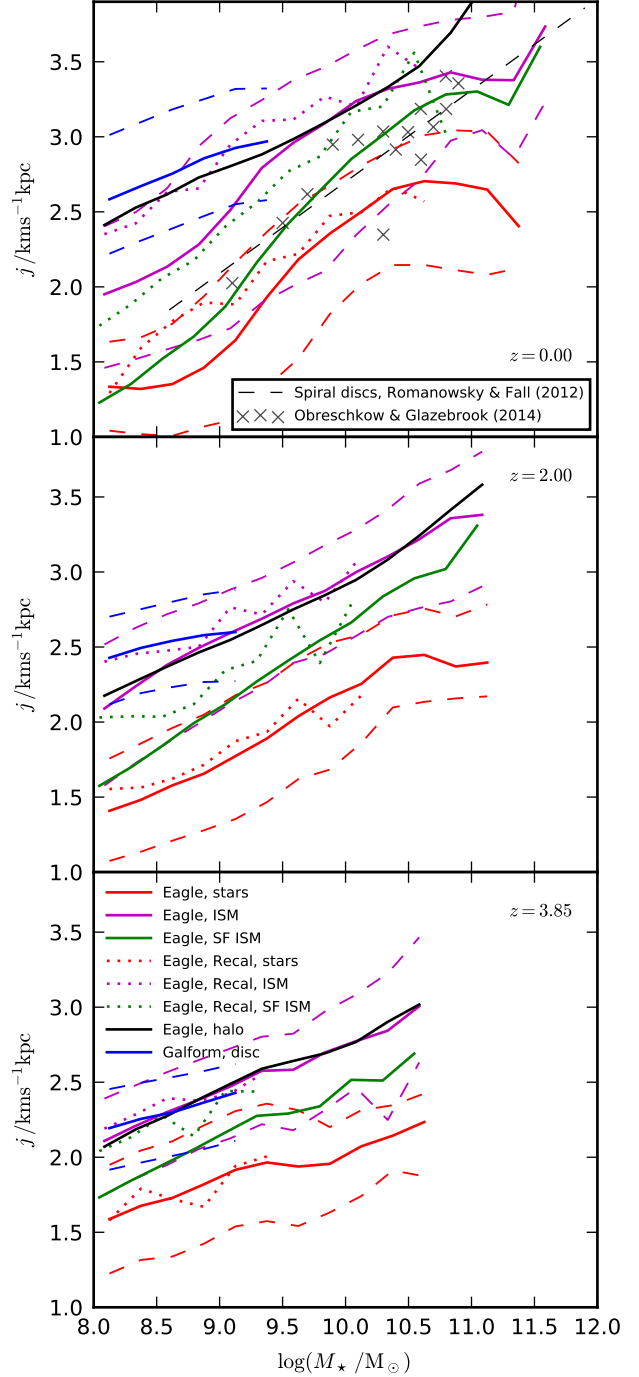


Figure 7. Specific stellar angular momentum as a function of stellar mass. Red and blue lines show respectively the distributions of stellar specific angular momentum from the reference EAGLE and GALFORM models. For GALFORM, we only show stellar mass bins that are disc dominated (such that stellar specific angular momentum is well defined in the model). Magenta and green lines show respectively the distributions of total ISM and star-forming ISM specific angular momentum from the reference EAGLE simulation. Solid lines show the medians and dashed lines show the 16 and 84th percentiles of the distributions. Dotted red, magenta and green lines show respectively the corresponding median angular momenta from the higher resolution, recalibrated EAGLE simulation. Solid black lines show the median specific angular momentum of dark matter haloes at a given stellar mass in EAGLE. Grey points show galaxies from the THINGS survey (Obreschkow & Glazebrook 2014). The grey dashed line shows the power-law fit to the distribution of disc specific angular momentum from Romanowsky & Fall (2012). Each panel corresponds to a different redshift, as labelled.

¹⁰ We emphasise that we have not internally modified the GALFORM model to perform this calculation, and as such the distribution (and many other predictions of the model) would likely look different if we were to do so.

hosting dark matter haloes (black lines). Interestingly, the specific angular momentum of the ISM in the EAGLE reference model dips below the halo specific angular momentum for low-mass galaxies at $z = 0$. This is not the case at $z = 2, 4$ and the $z = 0$ feature disappears in the recalibrated EAGLE model (dotted magenta lines). This difference is presumably related to the much higher gas ratios predicted by this variant model for low-mass galaxies at $z = 0$ (and hence the convergence issues seen in Fig. 5).

To make a comparison between GALFORM and EAGLE in Fig. 7 for total specific stellar angular momentum (blue and red lines), we must account for the problem that GALFORM does not model the angular momenta of galaxy bulges/spheroids. This is particularly an issue for massive galaxies (which have high bulge-to-total ratios). For GALFORM, we therefore choose to show disc specific angular momentum rather than total specific angular momentum and to only show the distribution for stellar mass bins where at least 70% of the galaxies are disc dominated ($M_{\text{disc}}/M_{\text{disc}} + M_{\text{bulge}} > 0.7$).

In contrast to EAGLE, GALFORM (blue lines) assumes that the ISM and stars have the same specific angular momenta in galaxy discs. Fig. 7 shows that the median stellar specific angular momentum of disc-dominated galaxies in GALFORM can be over an order of magnitude larger than in EAGLE at a given stellar mass. In GALFORM, disc-dominated galaxies have almost the same stellar (and ISM) specific angular momentum as the hosting dark matter haloes (black lines). The corresponding galaxies in EAGLE have much lower specific stellar angular momentum than their host haloes. On the other hand, the specific angular momentum of the total ISM in EAGLE is in good agreement with the specific angular momentum of GALFORM discs (and so in agreement with the specific angular momentum of the ISM in GALFORM discs).

At $z = 0$, we also show observational data for specific stellar angular momentum of gas-rich spiral galaxies from Romanowsky & Fall (2012) and Obreschkow & Glazebrook (2014). As discussed by Lagos et al. (2017b), when selecting EAGLE galaxies with high gas fractions, EAGLE agrees with the observations quite well, because gas-rich galaxies have higher specific stellar angular momentum at a given stellar mass. In contrast, GALFORM predicts a stellar specific angular momentum which (with some extrapolation of the observations) is too high for low-mass galaxies. This picture is consistent with the GALFORM overprediction of low-mass galaxy sizes in the local Universe (see Appendix D). Put together, this serves to underline that self-consistently computing the angular momentum of newly-formed stars from centrally-concentrated (low-angular momentum) star-forming gas in the ISM is likely a needed ingredient for future semi-analytic models.

Finally, we note here that the specific angular momentum of the ISM and stars in EAGLE is (to some extent) sensitive to the assumed model parameters. For example, increasing the normalisation of the star formation law in EAGLE (see Appendix A2) increases slightly the ISM specific angular momentum (not shown here), as well as lowering the ISM-to-stars mass fraction (Crain et al. 2017). A simple interpretation of this trend is that increasing the assumed star formation efficiency depletes more of the star-forming ISM (by star formation and feedback driven outflows), increasing the relative importance of the non-star-forming ISM, which is less centrally concentrated and so has higher specific angular momentum.

6 FEEDBACK

6.1 Stellar feedback, AGN feedback and gas return timescales

In EAGLE, stellar feedback is implemented locally by injecting thermal energy into gas particles which neighbour young star particles (Schaye et al. 2015). Gas particles are heated by a fixed temperature difference, $\Delta T = 10^{7.5}$ K, which acts to suppress artificial radiative losses (Dalla Vecchia & Schaye 2008). The average injected per supernova explosion is scaled as a function of gas density and metallicity, ranging between 0.3 and 3 times the canonical energy of 10^{51} ergs (with a mean value very close to the canonical value) (Crain et al. 2015). In GALFORM, stellar feedback is implemented globally across a given galaxy by ejecting gas from galaxies (and haloes) with an efficiency that scales with galaxy circular velocity. More details of this modelling, as well as a discussion of the energetics of stellar feedback in GALFORM, are given in Appendix A4.

In EAGLE, AGN feedback is implemented similarly to stellar feedback, but with a heating temperature of $\Delta T = 10^{8.5}$ K (an order of magnitude higher than for stellar feedback) and with a fixed average efficiency (relative to the SMBH accretion rate). In principle, this model of AGN feedback can both heat gas in the ISM and in the halo, and remove gas entirely from haloes. In GALFORM, AGN feedback acts only to prevent gas infall from the halo onto galaxy discs, and does not eject gas from haloes. AGN feedback is activated in GALFORM if the SMBH injects sufficient energy to balance radiative cooling in the halo, and if the halo is considered to be in a quasi-hydrostatic state. Further details of this modelling, and of the modelling of SMBH seeding and growth, are presented in Appendix A5. We compare the GALFORM and EAGLE distributions of black hole mass as a function of stellar mass in Appendix E, where we show that GALFORM does not predict the steep dependence on stellar mass predicted by EAGLE at $z = 2, 4$.

Arguably, the most important uncertainty in semi-analytic galaxy formation models is the fate of outflowing gas that is ejected from galaxies by feedback (e.g. Henriques et al. 2013; Mitchell et al. 2014; White et al. 2015; Hirschmann et al. 2016). In GALFORM, this ejected gas is placed into a distinct reservoir and is assumed to return to the diffuse gas halo over a halo dynamical time (see Appendix A6). While the spatial location of this ejected gas is not formally defined, we choose to the interpretation that this gas is outside the halo virial radius (see Appendix A6). Given that the halo dynamical time is always approximately equal to 10% of the age of the Universe at a given epoch (independent of halo mass), ejected gas is rapidly reincorporated back into the diffuse gas halo in GALFORM. This rapid gas cycling (infall timescales from the diffuse halo onto the disc are also typically of order a halo dynamical time) forces the model to employ very large mass-loading factors in order to explain the low observed efficiency of cosmic star formation. This is common to some other semi-analytic models (e.g. Springel et al. 2001), although see also Somerville et al. (2008b); Hirschmann et al. (2016).

Importantly, it is assumed in GALFORM that AGN feedback does not eject gas from galaxies (or from haloes), and instead acts only to suppress radiative cooling from the diffuse gas halo. Given the fairly short reincorporation timescale assumed in GALFORM, this means that the baryon cycle (infall, ejection, reincorporation) effectively ceases and the halo baryon fraction rapidly reaches the cosmic mean once AGN feedback becomes active in a given halo (although see Monaco et al. 2007; Bower et al. 2008; Somerville et al. 2008b; Bower et al. 2012, for alternative schemes where AGN can eject gas from haloes).

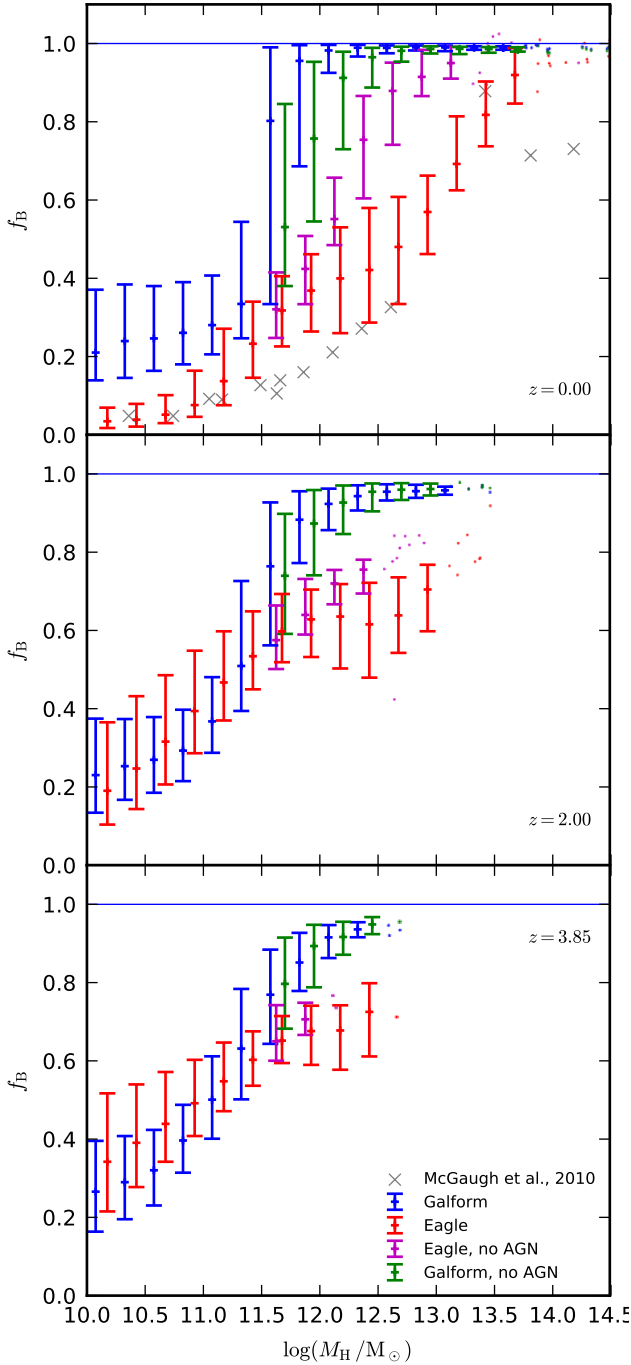


Figure 8. Baryon fractions within the halo virial radius for central galaxies as a function of halo mass. Baryon fractions are defined relative to the universal baryon fraction, with a value of unity (blue horizontal line) indicating that the halo contains the universal baryon fraction. Red and blue points with error bars show the distributions from the reference EAGLE and GALFORM models respectively. In the mass range where they start to differ from the reference models, green and magenta points with error bars show the distributions from GALFORM and EAGLE respectively for models that do not include AGN feedback. The points with errorbars show the 16, 50 and 84th percentiles of the distributions. The small coloured points without error bars show individual central galaxies in bins containing few galaxies. Grey crosses show the baryonic inventory compilation from McGaugh et al. (2010). Each panel corresponds to a different redshift, as labelled.

In hydrodynamical simulations, gas flows are predicted locally by self-consistently following gravity and hydrodynamics. As such, they do not make any explicit assumptions for gas return timescales. Implicitly however, simulations set the return time through the details of the subgrid models for feedback. In the case of EAGLE, outflowing particle trajectories will be sensitive to the assumed feedback heating temperature. In hydrodynamical simulations without an explicitly assumed wind speed (and in reality), gas is presumably ejected from galaxies with a broad distribution of energies (e.g. Christensen et al. 2016). Correspondingly, it is to be expected there will be a distribution of return timescales among gas particles associated with a wind, ranging from short timescales (less than a Hubble time, as in GALFORM) to timescales much longer than a Hubble time, such that the gas effectively never returns (Oppenheimer et al. 2010; Christensen et al. 2016; Anglés-Alcázar et al. 2017; Crain et al. 2017). It is not clear therefore whether the total return rate should be linear in the mass of the ejected gas reservoir (as assumed in GALFORM, Eqn A7), or whether the return rate will tightly correlate with halo properties, as is assumed in semi-analytic models.

6.2 Halo baryon fractions

While we do not measure mass-loading factors or gas return timescales from EAGLE for this study (we defer this to future work), an indirect measure of the efficiency of these processes is given simply by the mass fraction of baryons within the virial radii of dark matter haloes. Fig. 8 shows the baryon fractions as a function of halo mass for a range of redshifts. For all models, the baryon fractions rise from low values in small haloes to high values in massive haloes, implying that to first order the baryon cycles in the two models are similar. However, in detail there are various qualitative differences.

At a characteristic halo mass of $M_H \approx 10^{12} M_\odot$, baryon fractions in GALFORM rapidly approach the cosmic mean. This transition is significantly more gradual in the reference EAGLE model, such that the baryon fraction approaches the cosmic mean only in galaxy clusters ($M_H \approx 10^{14} M_\odot$). For the models without AGN feedback (green and magenta points), there is still a difference between the two models for $M_H \geq 10^{12} M_\odot$, indicating that SNe feedback is more effective in EAGLE than in GALFORM in massive haloes (either because more gas is ejected or because gas takes longer to return). When AGN feedback is included, EAGLE and GALFORM show divergent behaviour. AGN feedback acts to reduce the baryon fractions (either by direct mass ejection or by preventing primordial accretion or gas return) in massive haloes in EAGLE. In GALFORM, AGN feedback does not eject gas and instead suppresses gas cooling, which in turn acts to suppress future SNe-driven outflows, resulting in higher baryon fractions than the no-AGN case.

In practice, suppressing cooling and ejecting gas from haloes will both act to suppress star formation. Accordingly, the differing baryon fractions in massive haloes between EAGLE and GALFORM will not necessarily result in differing stellar mass assembly histories. The ejection/non-ejection of baryons by AGN feedback is relevant to the predicted X-ray properties of massive haloes however, as explored in Bower et al. (2008).

In lower-mass haloes, below the regime where AGN feedback plays a role, the two models come into better agreement but still show a different evolution with redshift. At $z = 4$, SNe appear to be slightly more efficient in removing baryons in GALFORM than in EAGLE for the lowest-mass haloes shown. At $z = 2$, the models are

very comparable and by $z = 0$, EAGLE has a lower baryon fraction at a given halo mass in low-mass haloes.

At $z = 0$, Fig. 8 also shows the baryon inventory compilation from McGaugh et al. (2010), corrected to be consistent with halo masses defined relative to 200 times the critical density of the Universe. Both GALFORM and EAGLE agree with the basic qualitative trend of increasing baryon fraction with halo mass (see Haider et al. 2016, to see that this is not trivially the case in simulations). For low-mass haloes ($M_H < 10^{13} M_\odot$), the baryonic mass estimates presented in McGaugh et al. (2010) include contributions only from stars and the ISM, neglecting any CGM contribution (and so should be considered lower limits). In both GALFORM and EAGLE, a significant part of the baryonic mass always belongs to the CGM component, even in lower mass halos (see Section 7.1).

For the more massive haloes shown in the McGaugh et al. (2010) compilation, baryonic masses are instead inferred from X-ray measurements of galaxy groups and clusters. Here, a detailed self-consistent comparison with X-ray observations that takes into account observational biases and systematics has not been performed (and is beyond the scope of this paper). However, more detailed comparisons of EAGLE and GALFORM to group and cluster X-ray measurements have been presented in Bower et al. (2008), Schaye et al. (2015) and Schaller et al. (2015a). For GALFORM, Bower et al. (2008) found that the fiducial GALFORM model (similar to the one shown here) significantly overpredicts the X-ray emission from galaxy groups, and that this could be resolved in a variant model by expelling hot gas from haloes with AGN feedback. This simple picture is consistent with how EAGLE behaves. Schaye et al. (2015) and Schaller et al. (2015a) have compared EAGLE to the X-ray content of galaxy groups and clusters, using the methodology of Le Brun et al. (2014) to perform a self-consistent comparison. They find that the reference EAGLE model shown here overpredicts the hot gas content of galaxy groups by about 0.2 dex, and that this can be resolved by increasing the heating temperature for AGN feedback. The simple comparison shown here in Fig. 8 is consistent with this picture.

To summarise, we have shown in this section that the different implementations of SNe and AGN feedback in GALFORM and EAGLE lead to similar baryon fractions in lower-mass haloes, but very different baryon fractions in group-scale haloes. This is not necessarily important for stellar mass assembly but will have a strong impact on the X-ray properties of galaxy groups (Bower et al. 2008).

7 GALAXY EVOLUTION AND THE BARYON CYCLE

Here, we explore how the physical processes discussed in previous sections (star formation, feedback and gas cycling) shape galaxy evolution by presenting the baryonic assembly histories of galaxies in EAGLE and GALFORM.

The time evolution of the ejected gas reservoir discussed in Section 6.1 is shown explicitly in Fig. 9, in this case tracing the main progenitors of central galaxies with $9.75 < \log(M_*/M_\odot) < 10.25$ at $z = 0$. Green lines show the median ejected gas mass for the two models. Matched at this stellar mass at $z = 0$, central galaxies in EAGLE (dashed lines) on average have a higher mass fraction in the ejected reservoir at all redshifts than in GALFORM, and the mass in the ejected gas reservoir increases monotonically with time. In contrast, GALFORM (solid lines) predicts that the median mass in the ejected reservoir rises with time up until $z \approx 1.5$, before steadily declining until $z = 0$ (note the ejected reservoir does not include ejected gas which has been subsequently rein-

corporated). This is a result of the short return timescale assumed in GALFORM, whereby the ejected gas reservoir closely traces the evolution of mass in the ISM (solid blue line). In EAGLE, the evolution of the ISM mass (dashed blue line) is fairly steady with time, rising to a peak and then modestly declining until $z = 0$. The contrast between the evolution of the ISM (slow decline) and ejected gas reservoir (gradual rise) for $z < 1$ indicates that the net return timescale is likely longer in EAGLE than is assumed in GALFORM. This interpretation is supported by Crain et al. (2017), who saw no evidence for gas particles directly heated by feedback returning to galaxies at later times in EAGLE (after inspecting past phase diagrams of gas particles selected at a given epoch).

The stellar mass assembly histories (black lines) are in very good agreement between the two models in this mass bin. Such a level of agreement does not extend to any of the gas reservoirs however. This serves to underline that the stellar assembly histories of galaxies are not enough to constrain the feedback processes in galaxy formation models. In particular, the median mass in the diffuse gas halo is a factor 4 larger on average in GALFORM compared to EAGLE. Importantly, the full distribution of masses in the diffuse gas halo (not shown) is significantly wider in GALFORM. We return to this issue in Section 8 when discussing the infall/cooling model used in GALFORM.

The upper-right panel of Fig. 9 shows the star formation (cyan) and stellar mass assembly histories (time derivative of the stellar mass, shown in black) of the same selection of galaxies. The peak of star formation is slightly later in EAGLE with respect to GALFORM, which leads to better agreement with the observed decline in specific-star formation rates (Mitchell et al. 2014; Furlong et al. 2015). In Mitchell et al. (2014), it was demonstrated that such a delay in the star formation peak is only possible by introducing a very strong redshift evolution in the gas-return timescale or mass-loading factor, significantly beyond what is possible in the standard GALFORM parameter space. Interestingly, there is also a small contribution in EAGLE from star formation that takes place outside the ISM (yellow line), a possibility that is not considered in GALFORM. Visually (see Fig. C2), we find that radially-infalling star-forming gas can start to fragment and form stars before settling into rotational equilibrium closer to the halo centre.

The lower-left panel of Fig. 9 shows the evolution in specific angular momentum of different baryonic components. Specific angular momentum increases monotonically with cosmic time for all components in both models, in accordance with tidal torque theory Catelan & Theuns (1996), (see Lagos et al. 2017b, for an analysis of in the context of EAGLE). Interestingly, there is a much greater level of segregation in specific angular momentum between different baryonic components in EAGLE compared to GALFORM. In GALFORM, angular momentum is conserved for gas infalling onto galaxies. Furthermore, it is assumed that outflowing gas ejected by SNe feedback has the same specific angular momentum as the overall ISM. Consequently, the ISM (solid-blue line) has very similar specific angular momentum to the diffuse gas halo (solid-red line) as it evolves. The stellar specific angular momentum (solid black line) is not fully defined in GALFORM (see Section 5) because the angular momentum of galaxy bulges is not tracked. We choose to set the bulge angular momentum to zero. The resulting stellar specific angular momentum should therefore be regarded as a lower limit (as bulges/spheroids do rotate). Even as a lower limit however, the stellar specific angular momentum in GALFORM is still significantly higher than in EAGLE.

In EAGLE, the ISM and the stellar components abruptly decouple in specific angular momentum at redshift ≈ 6 , after which

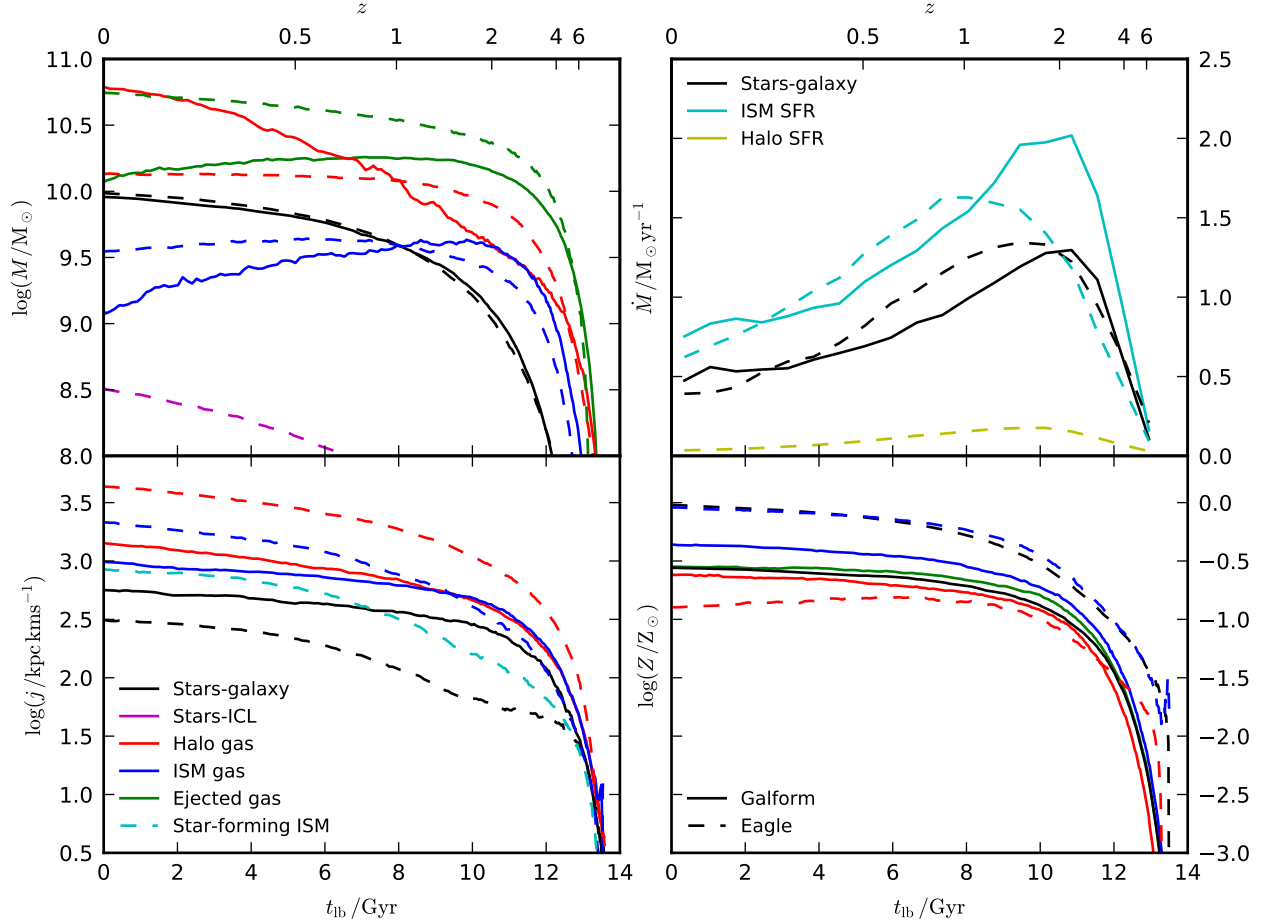


Figure 9. Baryonic assembly histories as a function of lookback time for central galaxies with stellar masses in the range, $9.75 < \log(M_*/M_\odot) < 10.25$, at $z = 0$. Here, the main progenitors of galaxies selected at $z = 0$ are traced backwards in time. Different line colours correspond to different baryonic components, as labelled. Solid lines show the average histories from GALFORM. Dashed lines show the corresponding histories from EAGLE. *Top-left:* Median mass in different baryonic components. *Top-right:* Mean time derivative of the stellar mass (black), and mean ISM (cyan) and non-ISM (halo SFR, yellow) star formation rates. Note that this panel is shown on a linear scale. *Bottom-left:* Median specific angular momentum in different baryonic components. For GALFORM, we set the (otherwise undefined) specific angular momentum of galaxy bulges to zero. The average stellar disc specific angular momentum in GALFORM is identical to that of the ISM (solid blue line). For EAGLE only, we also show the specific angular momentum of the star-forming ISM in this panel (cyan dashed line). *Bottom-right:* Median metallicity in different baryonic components.

the ISM has a factor ≈ 6 larger specific angular momentum. The transition redshift marks the point at which the star-forming ISM (dashed cyan line) starts to decouple from the total ISM. It also marks the point at which the previously formed stellar mass is significant enough that the past average specific angular momentum (represented by the stars) drops below the ISM value.

Another interesting feature of the lower-left panel of Fig. 9 is that the halo gas specific angular momentum (dashed red line) in EAGLE is positively offset with respect to the ISM (by a factor ~ 2.5 at $z = 0$). This behaviour is not predicted to the same extent by GALFORM, and not at all for $z > 1$. This closer coevolution of the ISM and halo gas in GALFORM stems first from the assumption that angular momentum of gas is conserved as it condenses from the halo component onto a galaxy disc. Secondly, infall rates onto galaxy discs in GALFORM are high enough in the non-quasi-hydrostatic regime that all of the halo gas at a given epoch will be accreted onto the disc. The segregation of specific angular momentum between these components in EAGLE is therefore suggestive that angular momentum is either not exactly conserved for

infalling material (see Stevens et al. 2017, for a similar conclusion), or that infalling material is preferentially low-angular momentum compared to the overall halo gas reservoir. It also seems likely that infall rates may be lower than in GALFORM, such that more radially distant, high angular momentum gas is never accreted onto galaxies.

The lower-right panel of Fig. 9 shows the evolution in metallicity for different baryonic components. GALFORM predicts that the median metallicity in each component closely traces each of the others with the median ISM metallicity positively offset by 60% from stellar metallicity at $z = 0$. In contrast, EAGLE predicts that the ISM and stellar components have almost identical metal content at $z = 0$ and co-evolve very closely (the upturn at high-redshift in the ISM metallicity is caused by galaxies dropping out of the sample as they can no longer be identified by the halo finder, with the remaining galaxies probably being unusually metal enriched at these redshifts). EAGLE also predicts that the diffuse halo gas component is negatively offset in metallicity by a factor that grows fractionally with time, reaching a factor ≈ 7 by $z = 0$.

In GALFORM, metals are exchanged between different components such that they linearly trace the total baryonic mass exchange. As such, it is assumed that the metal-loading factor (ratio of metal ejection rate from the ISM to the rate with that ISM metals are locked into stars by star formation) is the same as the mass-loading factor. This need not be the case (e.g. Creasey et al. 2015; Lagos et al. 2013). Furthermore, GALFORM assumes that newly-formed stars form with the metallicity of the total ISM component, neglecting any possible radial gradients that could lead to differences between the average metallicity of star-forming gas and total ISM. Combined with the difference in mass exchange rates implied by the contrasting predictions shown in the upper-left panel of Fig. 9, it is therefore somewhat challenging to interpret the differences in metal evolution between the two models. That the diffuse gas halo metallicity is significantly lower in EAGLE than the ISM and stellar components does suggest that considerably less baryon cycling is taking place compared to GALFORM, suggesting a longer gas return timescale.

7.1 Mass dependence

Fig. 10 shows the same information as the upper-left panel of Fig. 9 but plotted for a range of stellar mass bins. Overall, the two models come into better agreement for lower mass galaxies ($M_\star = 10^9, 10^{9.5} M_\odot$) but increasingly disagree for more massive galaxies ($M_\star = 10^{10.5}, 10^{11} M_\odot$). For the lower mass galaxies, the ejected gas reservoir dominates the mass budget in both models. The stellar mass in these galaxies forms later in GALFORM and GALFORM contains systematically higher ISM content at all redshifts, presumably resulting in more prolonged star formation histories.

For more massive galaxies (lower panels), the two models quickly start to diverge at high-redshift in the mass of the ejected gas reservoir. In GALFORM, the ejected gas reservoir mass peaks at $z \approx 3$ before steadily declining down to $z = 0$. In EAGLE, the ejected gas reservoir mass does not peak and continues to rise until low-redshift and is always comparable to, or greater in mass than the diffuse halo gas component. In GALFORM, the diffuse halo component completely dominates over the ejected gas reservoir by $z = 0$. As shown in Fig. 8, this primarily reflects the different implementations of AGN feedback in the two models.

It is also notable that the total baryonic mass is significantly larger in EAGLE than in GALFORM for the higher mass stellar mass bins shown. In this stellar mass range, the $M_\star - M_H$ relation is shallow, such that a small difference in stellar mass leads to a large difference in halo mass (see Fig. 1). Given that we match galaxy samples here at a fixed stellar mass, the difference in total baryonic mass for the two models is therefore primarily driven by the difference in host halo mass at a fixed stellar mass. The difference in halo mass definition also contributes (see Appendix B).

7.2 The mass-loading / return-time degeneracy

In Mitchell et al. (2014) and Rodrigues et al. (2017) it was demonstrated that there is a degeneracy between gas return timescale and mass-loading factor in GALFORM if the model is calibrated to reproduce a given stellar mass function (see also Somerville et al. 2008b). Intuitively, a higher mass-loading factor (more gas ejected from galaxies) can be compensated for by increasing the rate of gas return, ultimately leading to very similar stellar mass growth histories. This is explicitly demonstrated in Fig. 11, which shows

three GALFORM models. The first is the fiducial reference model for this study (solid lines) with the return time parameter, $\alpha_{\text{return}} = 1.26$ and the mass-loading factor normalization parameter set to $V_{\text{SN}} = 380 \text{ km s}^{-1}$. The other two models shown were run with $\alpha_{\text{return}} = 8$, $V_{\text{SN}} = 650 \text{ km s}^{-1}$ (strong SNe feedback and rapid gas return, dotted lines) and $\alpha_{\text{return}} = 0.4$, $V_{\text{SN}} = 300 \text{ km s}^{-1}$ (weak SNe feedback and slow gas return, dash-dotted lines).

While the three GALFORM models shown predict very similar stellar mass assembly histories, the median mass in the ejected gas reservoir ranges over almost an order of magnitude by $z = 0$. Notably, the model with slow gas return and smaller mass-loading factors is in closer agreement with EAGLE for the evolution in mass of the ejected gas reservoir, further increasing the evidence that return timescales are likely longer in EAGLE than are typically assumed in semi-analytic galaxy formation models. We note also that adopting a longer return timescale alleviates the tension in our reference model that likely unrealistic amounts of energy are implicitly injected into SNe-driven winds, as discussed in Section 6.1. Interestingly, Rodrigues et al. (2017) show that when higher-redshift stellar mass functions are included as constraints, values of $\alpha_{\text{return}} < 0.4$ are strongly disfavoured. Presumably, this tension could probably be alleviated by using a scale dependent gas return timescale, as advocated by Henriques et al. (2013).

To summarise, we have seen several indications in this section that the level of baryon cycling after gas is blown out of galaxies by feedback is lower in EAGLE than in GALFORM. This supports the preliminary conclusion by Crain et al. (2017) that there appears to be little ejected gas return in EAGLE. Evidence here supporting this viewpoint comes from the significantly increased segregation in metallicity between halo gas and ISM gas in EAGLE compared to GALFORM and the lack of a close coevolution between the ISM and ejected gas reservoirs in EAGLE (compared to GALFORM). Finally, increasing the ejected gas return timescale in GALFORM improves the agreement with EAGLE in baryonic mass assembly histories.

8 RADIATIVE COOLING AND INFALL

In GALFORM, gas infalls from the diffuse gas halo onto the galaxy disc at a rate which is controlled by the minimum of two physical timescales. The first is the radiative cooling timescale of hot halo gas and the second is the gravitational freefall timescale (Cole et al. 2000; Bower et al. 2006). The limiting timescale is then compared to the time elapsed since the previous halo mass-doubling event in order to decide how much gas cools at the current timestep. Further details of the gas infall model are presented in Appendix A7.

In the regime where enough time has passed since the previous mass-doubling event for all of the halo gas to both cool and freefall onto the galaxy disc, the gas infall rate is simply set equal to the accretion rate of diffuse gas onto the halo. The opposite regime occurs when AGN feedback becomes active in a given halo, completely suppressing gas infall if the halo is considered to be quasi-hydrostatic. The hydrostatic equality criterion used also depends on the time which has elapsed since the previous halo mass-doubling event (Bower et al. 2006).

We find that both of these regimes appear to play an active role in regulating the baryonic mass assembly in individual haloes in GALFORM. This is shown directly for three example haloes in Fig. 12. Halo mass doubling events (vertical grey lines) are followed by a characteristic pattern. Gas rapidly infalls from the diffuse gas halo onto the disc until either another mass-doubling event occurs or cooling abruptly stops (AGN feedback becomes active).

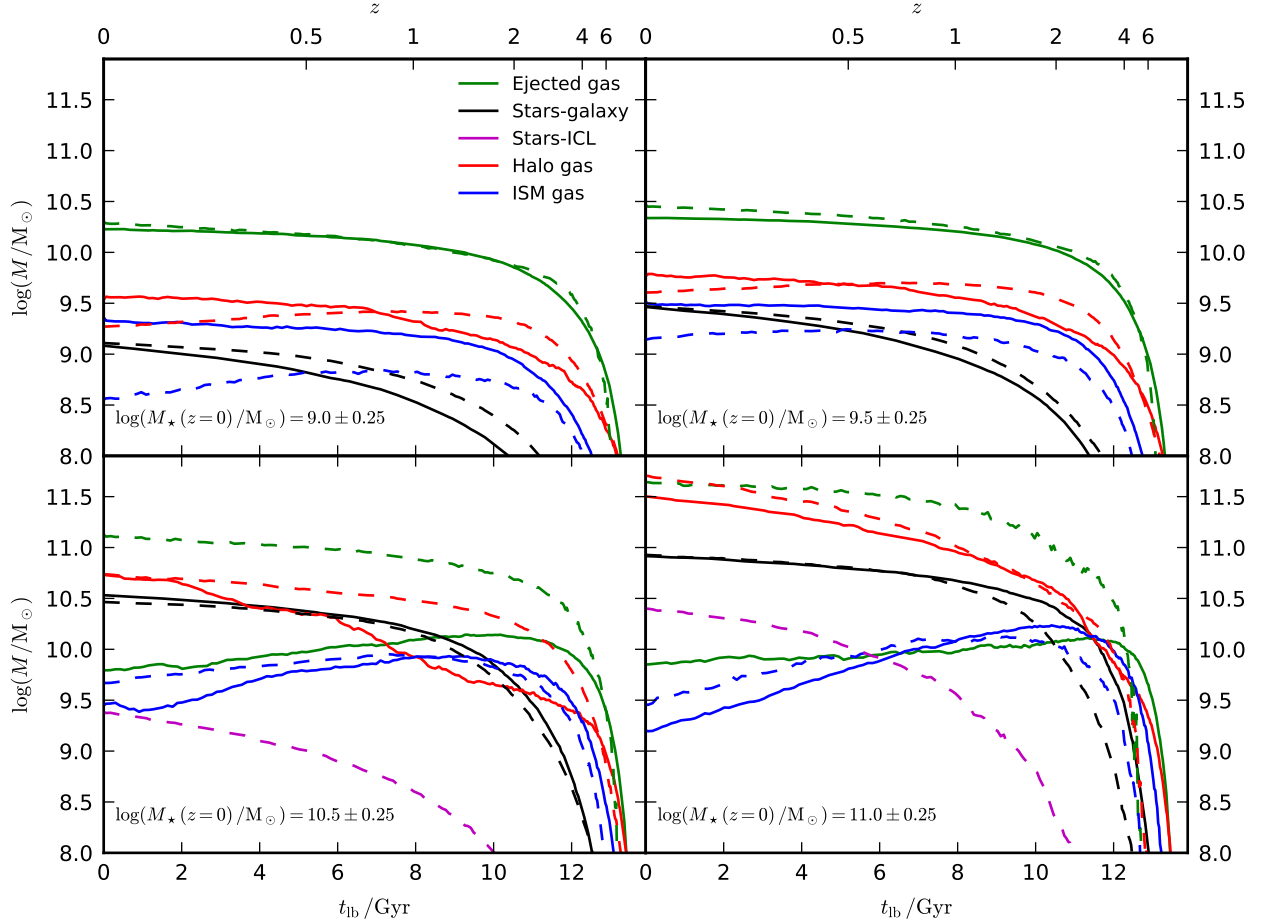


Figure 10. Median baryonic mass assembly histories for central galaxies. Each panel corresponds to a different stellar mass bin selected at $z = 0$, as labelled. Line formatting follows Fig. 9.

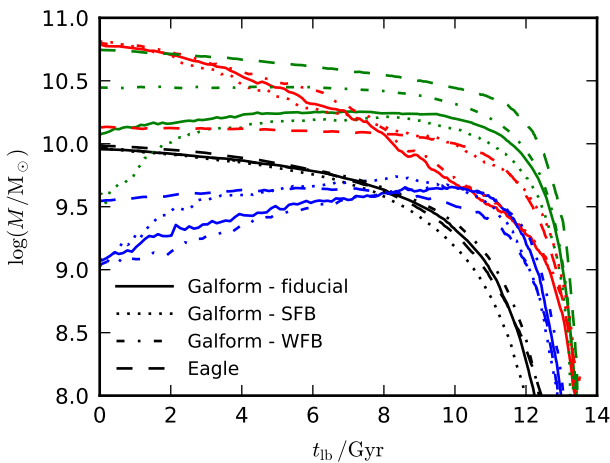


Figure 11. Median baryonic mass assembly histories for central galaxies with stellar masses in the range $9.75 < \log(M_*/M_\odot) < 10.25$, at $z = 0$. Solid lines show the fiducial GALFORM model. Dotted lines show a GALFORM variant model with strong SNe feedback (SFB) and rapid gas cycling. Dash-dotted lines a GALFORM variant model with weak SNe feedback (WFB) and slow gas cycling. Dashed lines show the EAGLE reference model. Otherwise, line formatting follows Fig. 9.

In some cases, there is sufficient time before one of these situations occur such that the diffuse gas halo is almost completely depleted (the diffuse gas halo mass never falls to exactly zero because of details in the numerical scheme, and instead fluctuates around a low floor value), corresponding to the regime where $r_{\text{infall}} > r_{\text{H}}$.

The result of this abrupt switching between regimes is the strongly oscillatory behaviour seen for the mass in different baryonic components shown in Fig. 12. Such behaviour is not seen for the corresponding individual haloes shown in EAGLE. We deliberately select three haloes to highlight the three possible cases for how well the stellar mass agrees between the two models at $z = 0$. In the top panel, GALFORM underpredicts the stellar mass at $z = 0$ by a factor ≈ 3 compared to EAGLE. In this case, the halo does not undergo a halo mass doubling event below $z \approx 1.5$, such that AGN feedback is able to completely suppress gas infall after $z \approx 0.6$, preventing the star formation that the corresponding EAGLE galaxy undergoes during this period. In the bottom panel, GALFORM overpredicts the stellar mass by the same factor compared to EAGLE, in this case because a halo mass-doubling event occurs late enough to allow significant late star formation but not so late that AGN feedback has a significant effect at late times. In the middle panel, the two galaxies agree in stellar mass simply because the final halo-mass doubling event in GALFORM fortuitously occurs at the right

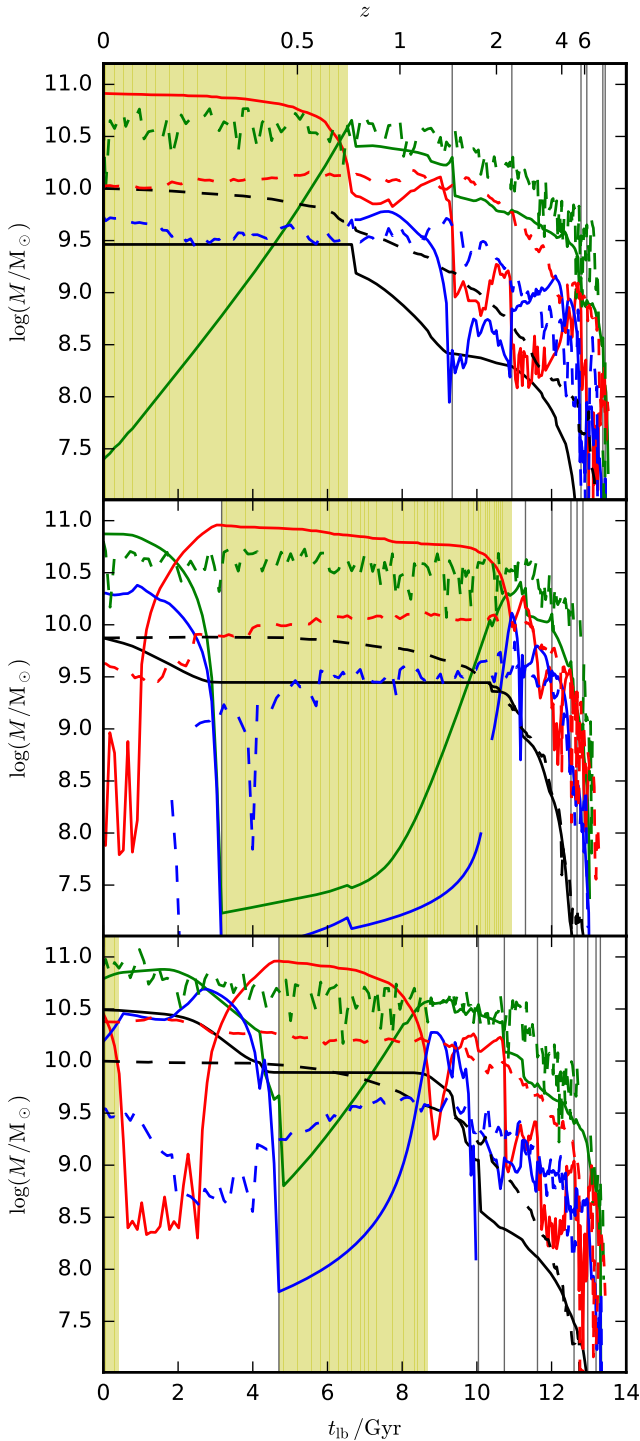


Figure 12. Median baryonic mass assembly histories for examples of individual central galaxies, matched between EAGLE and GALFORM. Each panel corresponds to a different galaxy. The galaxies were selected to high-light cases where GALFORM predicts lower, equivalent and higher stellar mass compared to EAGLE in the top, middle and bottom panels respectively. Line formatting follows Fig. 9. Vertical grey lines show halo mass-doubling events in GALFORM. Yellow shaded regions indicate when AGN actively suppress cooling from the diffuse gas halo in GALFORM.

time to allow the stellar mass to grow enough to match EAGLE at $z = 0$.

In summary, an artificial dependence on halo mass-doubling events and a bimodal model for AGN feedback (no effect or complete suppression of gas infall onto the disc), combined with strong SNe feedback and short return times leads to strongly oscillatory behaviour in GALFORM. This behaviour is not seen in EAGLE, for which it is not necessary to make any of these assumptions, instead allowing the associated physical phenomena to emerge naturally (albeit with uncertain local subgrid modelling for cooling rates and energy injection from AGN). This strongly suggests that both the cooling and AGN feedback models in GALFORM could be improved with the goal of eliminating this oscillatory behaviour (Hou et al., in prep, see also Benson & Bower 2010). In future work, we will directly compare the inflow rates between the two models to address this topic more directly.

8.1 Variable inflow rates and the scatter in stellar mass

In Fig. 13, we attempt to relate the oscillatory behaviour in inflow rates seen in Fig. 12 to the scatter in stellar mass between matched galaxies across the entire population shown in Fig. 2. The top panel shows that there is a strong positive correlation between the fraction, f_{SF} , of simulation outputs in which a main progenitor in GALFORM is considered a star-forming galaxy ($sSFR > 0.01 \text{ Gyr}^{-1}$) and the residual in stellar mass with the corresponding matched EAGLE galaxy. Galaxies with high f_{SF} in GALFORM form, on average, more stars than their eagle counterparts and GALFORM galaxies with low f_{SF} form fewer stars to compensate. This means a significant amount of the scatter seen in Fig. 2 can be attributed to star formation histories being more variable in GALFORM than in EAGLE.

The middle panel of Fig. 13 shows that there is not a corresponding correlation between the stellar mass residuals and the star-forming fraction, f_{SF} , measured in EAGLE. The lower panel of Fig. 13 reveals that this is because the only galaxies in EAGLE with low f_{SF} are massive ($M_* > 10^{10.5} M_\odot$) and so also have low f_{SF} in GALFORM. Conversely, there are galaxies in GALFORM with low f_{SF} at lower stellar masses ($M_* \approx 10^{10} M_\odot$). It is the variability of gas inflow rates in these lower mass galaxies (see Fig. 12) which are responsible for the strong correlation seen in the top panel of Fig. 13.

9 APPLICABILITY TO OTHER SEMI-ANALYTIC MODELS

Here, we briefly consider how the results from this study relate to other semi-analytic galaxy formation models used in the community. Several of the aspects of the modelling which we consider are specific to the details of the modelling in GALFORM, and cannot be easily generalised. We consider the oscillatory inflow rates tied to halo mass-doubling events and AGN feedback (seen in Fig. 8.1) as belonging to this category. Similarly, the effect of AGN feedback enhancing the baryon fractions of galaxy groups in GALFORM is specifically tied to the implementation of AGN feedback from Bower et al. (2006), and does not represent the behaviour of other semi-analytic models which include an explicit Quasar-mode of AGN feedback that can eject gas from haloes (e.g. Monaco et al. 2007; Somerville et al. 2008b; Croton et al. 2016).

Of more general interest is the importance of stars forming

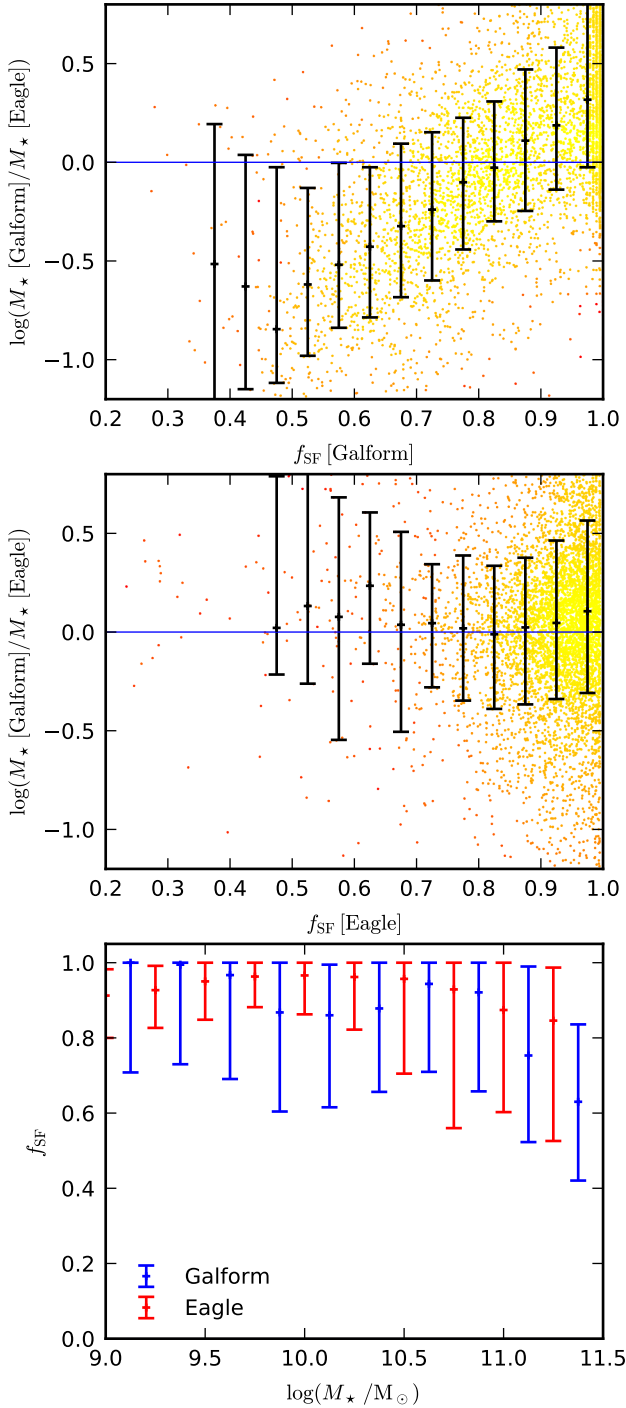


Figure 13. The connection between the scatter in stellar mass for matched GALFORM and EAGLE galaxies with star formation history. Galaxies included are central in both EAGLE and GALFORM at $z = 0$ and have $M_{\star} > 10^9 M_{\odot}$ in EAGLE. *Top:* Logarithmic residual in stellar mass at $z = 0$, plotted as a function of star-forming fraction, f_{SF} in GALFORM. Star-forming fraction is defined as the fraction of simulation outputs along the main progenitor branch for which the main progenitor has a specific star formation rate, $s\text{SFR} > 0.01 \text{ Gyr}^{-1}$. Coloured points show individual galaxies. Black points with error bars show the 16, 50 and 84th percentiles of the distribution. *Middle:* Same but plotted as a function of star-forming fraction in EAGLE. *Bottom:* Star-forming fraction plotted as a function of stellar mass for GALFORM (blue) and EAGLE (red). In this panel, points indicate the 10, 50 and 90th percentiles of the distributions.

preferentially out of gas in the ISM with low specific angular momentum. Semi-analytic models currently assume that disc stars form with the same specific angular momentum of either the gas disc (Guo et al. 2011), or the entire disc (e.g. Cole et al. 2000; Springel et al. 2005; Somerville et al. 2008a; Tecce et al. 2010; Croton et al. 2016). For the specific case of the L-GALAXIES model, cross-matching Guo et al. (2016) with Appendix D shows that this model overpredicts the sizes of low-mass ($M_{\star} \approx 10^9 M_{\odot}$) galaxies by a factor ≈ 2 in the local Universe, consistent with GALFORM predictions.

Also of interest is the behaviour of gas flows both onto and out of galaxies. For example, a wide range of gas return timescales have been adopted in contemporary galaxy formation models. Recent models have assumed that gas returns over a halo dynamical time (Lacey et al. 2016), over a Hubble time (Somerville et al. 2008b; Hirschmann et al. 2016), or have adopted more complex parametrisations where the return time scales with halo mass or halo circular velocity (Guo et al. 2011; Henriques et al. 2013; White et al. 2015; Croton et al. 2016; Hirschmann et al. 2016), or where the return timescale is explicitly connected to halo growth (Bower et al. 2012). Mitchell et al. (2014) have also argued on empirical grounds that a yet more complex dependence of the gas return timescale (or SNe mass-loading factor) on halo mass, halo dynamical time, and redshift is required to reproduce the observed evolution of characteristic star formation rates at a given stellar mass. With this diversity of different models, the hints found here that EAGLE predicts a longer gas return time (compared to a halo dynamical time) are certainly of interest, albeit with the caveat that the return times are likely sensitive to the assumed heating temperature for SNe and AGN feedback.

With respect to previous comparison studies between semi-analytic models and hydrodynamical simulations, it is difficult to directly compare results, particularly because we have not measured gas cooling rates in EAGLE (but see Stevens et al. 2017). The factor ≈ 10 discrepancy between star formation efficiency reported by Hirschmann et al. (2012) between a set of hydrodynamical simulations and a semi-analytic model is not seen in Fig. 4 (although a 0.5 dex discrepancy in the medians is seen for massive galaxies at $z = 4$). This suggests that the typical star-forming gas densities of the hydrodynamical simulations analysed in Hirschmann et al. (2012) are larger than those in EAGLE, resulting in a larger disagreement with the semi-analytic model. This may be related to the EAGLE feedback model being highly effective in reducing the typical gas densities of the ISM in which SNe explode (Crain et al. 2015).

10 SUMMARY

Guo et al. (2016) presented a comparison between the GALFORM (and L-GALAXIES) semi-analytic galaxy formation model and the state-of-the-art EAGLE hydrodynamical simulations. They demonstrated that while the two models are calibrated to produce similar stellar mass functions at $z = 0$, the two models predict markedly different metallicity and galaxy size distributions as a function of stellar mass (see also Appendix D1 for a comparison of galaxy sizes).

Here, we increase the depth of the comparison by matching individual galaxies and by isolating a number of important aspects in the physical modelling. In particular, we have carefully assigned baryonic particles in EAGLE to baryonic reservoirs that correspond to those included in GALFORM. In future work, we plan to use the

framework introduced here to measure the various mass, metal and angular momentum exchanges between these reservoirs in EAGLE, enabling a direct comparison to the assumptions made in semi-analytic models pertaining to mass inflows, outflows and baryon cycling. Even without these measurements however, a number of interesting differences between the two modelling approaches are readily apparent at the level of detail presented here. Our main results are summarised as follows:

- In Fig. 2 of Section 3, we show that the scatter in stellar mass between matched galaxies in EAGLE and GALFORM is 0.37 dex at $z = 0$ and slowly decreases with increasing redshift. For comparison, the empirical semi-analytic galaxy formation model presented in Neistein et al. (2012) achieved an agreement with the OWLS simulations of 0.08 dex (Schaye et al. 2010). Clearly, the agreement between GALFORM and EAGLE could be significantly improved.

- In Fig. 3 of Section 4.1, we show that the star formation thresholds implemented in EAGLE and GALFORM lead (probably in conjunction with differing gas surface density distributions) to strongly differing predictions for the mass fraction of the ISM which is forming stars. This is particularly true for low-mass galaxies at low-redshift, for which GALFORM predicts that almost all of the hydrogen in the ISM is in the atomic phase and therefore not actively forming stars.

- In Fig. 4 of Section 4.2, we show that the spatially-integrated efficiency with which the star-forming ISM is turned into stars in EAGLE is close to a constant value at $z = 0$, consistent with what is assumed in GALFORM. However, the local density dependence of the Schmidt-like law implemented in EAGLE leads to a star formation efficiency that increases with redshift. EAGLE also predicts that at higher redshifts the star formation efficiency is mass-dependent, such that star formation is globally more efficient in more massive galaxies.

- EAGLE predicts that the star-forming ISM typically has significantly lower specific angular momentum than the total ISM, reflecting that it is more centrally concentrated (see Fig. 6 in Section 5). This is in contrast to GALFORM which implicitly assumes that star-forming gas has the same specific angular momentum as the total ISM. We show that this discrepancy could be at least partially alleviated if GALFORM were to self-consistently compute the angular momentum of star-forming gas using the radial profiles of atomic and molecular hydrogen.

- The stellar specific angular momentum distributions as a function of stellar mass are markedly different between GALFORM and EAGLE (see Fig. 7 in Section 5), although the interpretation is hindered because GALFORM does not track a specific angular momentum for stars in galaxy bulges/spheroids. For low-mass galaxies, GALFORM predicts that the specific angular momentum of galaxy discs is similar to that of their dark matter haloes (simply reflecting the assumptions of the model). In contrast, EAGLE predicts that while the ISM component of these galaxies is consistent with dark matter haloes (at least in the higher resolution, recalibrated model), the stellar angular momentum is lower than the ISM by 0.6 dex below $z \approx 6$.

- We show that the implementations of SNe feedback in EAGLE and GALFORM lead to similarly low baryon fractions in low-mass haloes ($10^{10} < M_{\text{H}}/M_{\odot} < 10^{11.5}$, see Fig. 8 in Section 6.2), which is the regime where AGN feedback does not play a role in the models.

- We show GALFORM predicts much higher baryon fractions in group-scale haloes ($M_{\text{H}} \sim 10^{13}$) than EAGLE (see Fig. 8 in Section 6.2). AGN feedback in GALFORM suppresses infall onto

galaxies but does not eject gas from haloes or prevent gas accretion onto haloes, leading to higher baryon fractions than when AGN feedback is not included. Conversely, including AGN feedback in EAGLE acts to reduce baryon fractions in group-scale haloes.

- We show that while the median stellar mass assembly histories of galaxies in the two models are similar, the mass in other baryonic reservoirs is predicted to evolve differently (see Fig. 9 in Section 7). In particular, GALFORM assumes that gas is rapidly returned to the diffuse gas halo after being ejected by SNe feedback, such that the ejected gas reservoir closely traces the evolution in the ISM reservoir. In EAGLE, these reservoirs do not show such a degree of coupling in their evolution, suggesting that the level of baryon cycling is significantly lower. Furthermore, the level of metal mixing into the diffuse gas halo is significantly lower in EAGLE than in GALFORM, suggesting a lower level of gas cycling. GALFORM can be brought into better agreement with EAGLE by using a longer gas return timescale.

- In Fig. 12 of Section 8, we show that the standard AGN and cooling models for gas infall onto galaxy discs implemented in GALFORM results in strongly oscillating infall rates for individual galaxies. This behaviour is not seen in EAGLE, and it contributes significantly to the scatter in stellar mass between matched galaxies in GALFORM (see Fig. 13). The oscillatory behaviour in GALFORM stems from the implementation of AGN feedback being bimodal (either complete suppression of cooling or no effect) and the artificial dependency of AGN feedback and gas infall rates on halo mass doubling events.

Put together, we conclude that while galaxy evolution proceeds in a broadly similar manner in semi-analytic galaxy formation models compared to hydrodynamical simulations, there are a number of important over-simplifications adopted in GALFORM (but not necessarily in other semi-analytic models). This leads to important differences when the two models are compared in detail. For example, the assumption that stars form with the same specific angular momentum as the ISM (rather than just the star-forming ISM component) has significant consequences for galaxy sizes (see Appendix D).

Crucially, we have not compared inflow rates, mass-outflow rates or gas return timescales with EAGLE in this study. We expect potentially significant differences in all these quantities when compared to GALFORM and we will address this in future work. Specifically, it remains to be seen whether the parametrisations adopted for different physical processes in GALFORM (for example, the mass loading factor associated with SNe feedback scales as a power law with galaxy circular velocity) are capable of reproducing the macroscopic behaviour predicted by state-of-the-art hydrodynamical simulations. Hydrodynamical simulations such as EAGLE do not necessarily provide an accurate representation of reality. For example, the dynamics of outflowing gas are sensitive to uncertain subgrid modelling. Arguably however, it ought still to be possible for models like GALFORM to reproduce their macroscopic behaviour once an appropriate choice of model parameters has been adopted. That this is indeed possible has already been demonstrated for a highly simplified model that replaces many physical considerations with a simple empirical fit to the OWLS simulations (Neistein et al. 2012). If a similar level of agreement to simulations can be achieved for a more physically motivated model, semi-analytic models can continue to be employed as useful tools for understanding galaxy evolution with confidence that they do not make unreasonable assumptions, particularly with regard to angular momentum and gas cycling.

ACKNOWLEDGEMENTS

We thank Joop Schaye for reading and providing comments that helped improve the clarity of this paper. PM acknowledges the LABEX Lyon Institute of Origins (ANR-10-LABX-0066) of the Universit  de Lyon for its financial support within the program “Investissements d’Avenir” (ANR-11-IDEX-0007) of the French government operated by the National Research Agency (ANR). This work was supported by the Science and Technology Facilities Council [ST/L00075X/1, ST/P000451/1]. This work used the DiRAC Data Centric system at Durham University, operated by the Institute for Computational Cosmology on behalf of the STFC DiRAC HPC Facility (www.dirac.ac.uk). This equipment was funded by BIS National E-infrastructure capital grant ST/K00042X/1, STFC capital grants ST/H008519/1 and ST/K00087X/1, STFC DiRAC Operations grant ST/K003267/1 and Durham University. DiRAC is part of the National E-Infrastructure. CL is funded by a Discovery Early Career Researcher Award (DE150100618).

REFERENCES

- Angl s-Alc zar D., Faucher-Gigu re C.-A., Kere  D., Hopkins P. F., Quataert E., Murray N., 2017, *MNRAS*, 470, 4698
- Baldry I. K. et al., 2012, *MNRAS*, 421, 621
- Behroozi P. S., Wechsler R. H., Conroy C., 2013, *ApJ*, 770, 57
- Benson A. J., 2014, *MNRAS*, 444, 2599
- Benson A. J., Bower R., 2010, *MNRAS*, 405, 1573
- Benson A. J., Bower R. G., Frenk C. S., Lacey C. G., Baugh C. M., Cole S., 2003, *ApJ*, 599, 38
- Berlind A. A., Weinberg D. H., 2002, *ApJ*, 575, 587
- Bigiel F. et al., 2011, *ApJ*, 730, L13
- Blitz L., Rosolowsky E., 2006, *ApJ*, 650, 933
- Booth C. M., Schaye J., 2009, *MNRAS*, 398, 53
- Booth C. M., Schaye J., 2010, *MNRAS*, 405, L1
- Boselli A., Cortese L., Boquien M., Boissier S., Catinella B., Lagos C., Saintonge A., 2014, *A&A*, 564, A66
- Bothwell M. S. et al., 2014, *MNRAS*, 445, 2599
- Bower R. G., Benson A. J., Crain R. A., 2012, *MNRAS*, 422, 2816
- Bower R. G., Benson A. J., Malbon R., Helly J. C., Frenk C. S., Baugh C. M., Cole S., Lacey C. G., 2006, *MNRAS*, 370, 645
- Bower R. G., McCarthy I. G., Benson A. J., 2008, *MNRAS*, 390, 1399
- Bower R. G., Schaye J., Frenk C. S., Theuns T., Schaller M., Crain R. A., McAlpine S., 2017, *MNRAS*, 465, 32
- Brown T., Catinella B., Cortese L., Kilborn V., Haynes M. P., Giovanelli R., 2015, *MNRAS*, 452, 2479
- Catelan P., Theuns T., 1996, *MNRAS*, 282, 436
- Catinella B. et al., 2010, *MNRAS*, 403, 683
- Cattaneo A. et al., 2007, *MNRAS*, 377, 63
- Chabrier G., 2003, *ApJ*, 586, L133
- Christensen C. R., Dav  R., Governato F., Pontzen A., Brooks A., Munshi F., Quinn T., Wadsley J., 2016, *ApJ*, 824, 57
- Cole S., Aragon-Salamanca A., Frenk C. S., Navarro J. F., Zepf S. E., 1994, *MNRAS*, 271, 781
- Cole S., Lacey C. G., Baugh C. M., Frenk C. S., 2000, *MNRAS*, 319, 168
- Conroy C., Wechsler R. H., Kravtsov A. V., 2006, *ApJ*, 647, 201
- Crain R. A. et al., 2017, *MNRAS*, 464, 4204
- Crain R. A. et al., 2015, *MNRAS*, 450, 1937
- Creasey P., Theuns T., Bower R. G., 2015, *MNRAS*, 446, 2125
- Croton D. J. et al., 2006, *MNRAS*, 365, 11
- Croton D. J. et al., 2016, *ApJS*, 222, 22
- Dalla Vecchia C., Schaye J., 2008, *MNRAS*, 387, 1431
- Dav  R., Thompson R., Hopkins P. F., 2016, *MNRAS*, 462, 3265
- Davis M., Efstathiou G., Frenk C. S., White S. D. M., 1985, *ApJ*, 292, 371
- De Lucia G., Tornatore L., Frenk C. S., Helmi A., Navarro J. F., White S. D. M., 2014, *MNRAS*, 445, 970
- Dolag K., Borgani S., Murante G., Springel V., 2009, *MNRAS*, 399, 497
- Driver S. P. et al., 2012, *MNRAS*, 427, 3244
- Dubois Y. et al., 2014, *MNRAS*, 444, 1453
- Elmegreen B. G., 1989, *ApJ*, 338, 178
- Font A. S. et al., 2008, *MNRAS*, 389, 1619
- Furlong M. et al., 2015, *MNRAS*, 450, 4486
- Gonzalez-Perez V., Lacey C. G., Baugh C. M., Lagos C. D. P., Helly J., Campbell D. J. R., Mitchell P. D., 2014, *MNRAS*
- Guo Q. et al., 2016, *MNRAS*, 461, 3457
- Guo Q. et al., 2011, *MNRAS*, 413, 101
- Haider M., Steinhauser D., Vogelsberger M., Genel S., Springel V., Torrey P., Hernquist L., 2016, *MNRAS*, 457, 3024
- H ring N., Rix H.-W., 2004, *ApJ*, 604, L89
- Helly J. C., Cole S., Frenk C. S., Baugh C. M., Benson A., Lacey C., 2003, *MNRAS*, 338, 903
- Henriques B. M. B., White S. D. M., Thomas P. A., Angulo R. E., Guo Q., Lemson G., Springel V., 2013, *MNRAS*, 431, 3373
- Hirschmann M., De Lucia G., Fontanot F., 2016, *MNRAS*, 461, 1760
- Hirschmann M., Naab T., Somerville R. S., Burkert A., Oser L., 2012, *MNRAS*, 419, 3200
- Jenkins A., 2010, *MNRAS*, 403, 1859
- Jiang L., Helly J. C., Cole S., Frenk C. S., 2014, *MNRAS*, 440, 2115
- Keller B. W., Wadsley J., Couchman H. M. P., 2016, *MNRAS*, 463, 1431
- Lacey C., Cole S., 1993, *MNRAS*, 262, 627
- Lacey C. G. et al., 2016, *MNRAS*, 462, 3854
- Lagos C. d. P. et al., 2015, *MNRAS*, 452, 3815
- Lagos C. d. P., Lacey C. G., Baugh C. M., 2013, *MNRAS*, 436, 1787
- Lagos C. D. P., Lacey C. G., Baugh C. M., Bower R. G., Benson A. J., 2011, *MNRAS*, 416, 1566
- Lagos C. d. P. et al., 2017a, *ArXiv e-prints*
- Lagos C. d. P., Theuns T., Stevens A. R. H., Cortese L., Padilla N. D., Davis T. A., Contreras S., Croton D., 2017b, *MNRAS*, 464, 3850
- Le Brun A. M. C., McCarthy I. G., Schaye J., Ponman T. J., 2014, *MNRAS*, 441, 1270
- Leroy A. K., Walter F., Brinks E., Bigiel F., de Blok W. J. G., Madore B., Thornley M. D., 2008, *AJ*, 136, 2782
- Li C., White S. D. M., 2009, *MNRAS*, 398, 2177
- Lu Y., Mo H. J., Lu Z., Katz N., Weinberg M. D., 2014, *MNRAS*, 443, 1252
- Malbon R. K., Baugh C. M., Frenk C. S., Lacey C. G., 2007, *MNRAS*, 382, 1394
- Matthee J., Schaye J., Crain R. A., Schaller M., Bower R., Theuns T., 2017, *MNRAS*, 465, 2381
- McConnell N. J., Ma C.-P., 2013, *ApJ*, 764, 184
- McGaugh S. S., Schombert J. M., de Blok W. J. G., Zagursky M. J., 2010, *ApJ*, 708, L14

Mitchell P. D., Lacey C. G., Baugh C. M., Cole S., 2016, *MNRAS*, 456, 1459

Mitchell P. D., Lacey C. G., Cole S., Baugh C. M., 2014, *MNRAS*, 444, 2637

Monaco P., Benson A. J., De Lucia G., Fontanot F., Borgani S., Boylan-Kolchin M., 2014, *MNRAS*, 441, 2058

Monaco P., Fontanot F., Taffoni G., 2007, *MNRAS*, 375, 1189

Moster B. P., Naab T., White S. D. M., 2013, *MNRAS*, 428, 3121

Moster B. P., Somerville R. S., Maulbetsch C., van den Bosch F. C., Macciò A. V., Naab T., Oser L., 2010, *ApJ*, 710, 903

Muratov A. L., Kereš D., Faucher-Giguère C.-A., Hopkins P. F., Quataert E., Murray N., 2015, *MNRAS*, 454, 2691

Neistein E., Khochfar S., Dalla Vecchia C., Schaye J., 2012, *MNRAS*, 421, 3579

Norberg P. et al., 2002, *MNRAS*, 332, 827

Obreschkow D., Glazebrook K., 2014, *ApJ*, 784, 26

Oppenheimer B. D., Davé R., Kereš D., Fardal M., Katz N., Kollmeier J. A., Weinberg D. H., 2010, *MNRAS*, 406, 2325

Planck Collaboration et al., 2014, *A&A*, 571, A16

Rahman N. et al., 2012, *ApJ*, 745, 183

Rahmati A., Pawlik A. H., Raicevic M., Schaye J., 2013, *MNRAS*, 430, 2427

Rodrigues L. F. S., Vernon I., Bower R. G., 2017, *MNRAS*, 466, 2418

Romanowsky A. J., Fall S. M., 2012, *ApJS*, 203, 17

Rosas-Guevara Y. M. et al., 2015, *MNRAS*, 454, 1038

Saintonge A. et al., 2011, *MNRAS*, 415, 32

Saro A., De Lucia G., Borgani S., Dolag K., 2010, *MNRAS*, 406, 729

Schaller M., Dalla Vecchia C., Schaye J., Bower R. G., Theuns T., Crain R. A., Furlong M., McCarthy I. G., 2015a, *MNRAS*, 454, 2277

Schaller M. et al., 2015b, *MNRAS*, 451, 1247

Schaye J., 2004, *ApJ*, 609, 667

Schaye J. et al., 2015, *MNRAS*, 446, 521

Schaye J., Dalla Vecchia C., 2008, *MNRAS*, 383, 1210

Schaye J. et al., 2010, *MNRAS*, 402, 1536

Shen S., Mo H. J., White S. D. M., Blanton M. R., Kauffmann G., Voges W., Brinkmann J., Csabai I., 2003, *MNRAS*, 343, 978

Simha V., Cole S., 2017, *MNRAS*, 472, 1392

Somerville R. S. et al., 2008a, *ApJ*, 672, 776

Somerville R. S., Hopkins P. F., Cox T. J., Robertson B. E., Hernquist L., 2008b, *MNRAS*, 391, 481

Springel V. et al., 2005, *Nature*, 435, 629

Springel V., White S. D. M., Tormen G., Kauffmann G., 2001, *MNRAS*, 328, 726

Stevens A. R. H., del P. Lagos C., Contreras S., Croton D. J., Padilla N. D., Schaller M., Schaye J., Theuns T., 2017, *MNRAS*

Stringer M. J., Brooks A. M., Benson A. J., Governato F., 2010, *MNRAS*, 407, 632

Tecce T. E., Cora S. A., Tissera P. B., Abadi M. G., Lagos C. D. P., 2010, *MNRAS*, 408, 2008

Trayford J. W. et al., 2015, *MNRAS*, 452, 2879

van der Wel A. et al., 2014, *ApJ*, 788, 28

Vogelsberger M. et al., 2014, *MNRAS*, 444, 1518

White C. E., Somerville R. S., Ferguson H. C., 2015, *ApJ*, 799, 201

Wiersma R. P. C., Schaye J., Theuns T., Dalla Vecchia C., Tornatore L., 2009, *MNRAS*, 399, 574

Yates R. M., Henriques B., Thomas P. A., Kauffmann G., Johansson J., White S. D. M., 2013, *MNRAS*, 435, 3500

Yoshida N., Stoehr F., Springel V., White S. D. M., 2002, *MNRAS*, 335, 762

APPENDIX A: MODELLING DETAILS

A1 Star formation threshold

In EAGLE, a local metallicity-dependent density threshold, n_{H}^* , is used to decide which gas particles are forming stars, given by

$$n_{\text{H}}^* = \min \left(0.1 \left(\frac{Z}{0.002} \right)^{-0.64}, 10 \right) \text{ cm}^{-3}, \quad (\text{A1})$$

where Z is the gas metallicity (Schaye et al. 2015). This threshold acts to prevent star formation taking place in diffuse and/or low metallicity gas, reflecting the physical connection between metallicity and the formation of a cold, molecular ISM phase that can fragment to form stars (Schaye 2004).

In GALFORM, the formation of a molecular phase is explicitly computed following empirical correlations inferred from observations (Lagos et al. 2011). Star formation is only allowed to occur in molecular gas, such that the star formation threshold reflects the atomic/molecular ISM gas decomposition. The mass fraction of molecular hydrogen, $R_{\text{mol}} \equiv \Sigma(H_2)/\Sigma(HI)$, is computed as a function of radius in galaxy discs by assuming a connection to the ambient pressure of the ISM in the mid-plane, P_{ext} , (Blitz & Rosolowsky 2006), as

$$R_{\text{mol}}(r) = \left(\frac{P_{\text{ext}}(r)}{P_0} \right)^{0.92}, \quad (\text{A2})$$

where P_{ext} is calculated assuming vertical hydrostatic equilibrium (Elmegreen 1989) and P_0 is a constant (Lagos et al. 2011). As such, the star formation threshold for discs in GALFORM is computed as a function of the radial surface density profile of gas and stars and contains no metallicity dependence. GALFORM also contains a distinct ISM component that represents nuclear gas that is driven into the galaxy centre by disc instabilities and galaxy mergers. All of the gas in this component is assumed to be in a molecular phase and is considered to be actively forming stars.

A2 Star formation law

In EAGLE, star-forming gas is turned into stars stochastically, sampling from a Kennicutt-Schmidt star formation law rewritten as a pressure law by assuming vertical hydrostatic equilibrium (Schaye & Dalla Vecchia 2008) such that the star formation rate is given by

$$\psi = \sum_i m_{\text{gas},i} A (1 \text{ M}_{\odot} \text{ pc}^{-2})^{-n} \left(\frac{\gamma}{G} f_g P_i \right)^{(n-1)/2}, \quad (\text{A3})$$

where $m_{\text{gas},i}$ is the gas particle mass, $\gamma = 5/3$ is the ratio of specific heats, G is the gravitational constant, f_g is the gas mass fraction (set to unity). A and n are treated as model parameters which are set following direct empirical constraints from observations (Schaye et al. 2015). The fiducial value of $n = 1.4$ is modified to 2 for hydrogen densities greater than $n_{\text{H}} = 10^3 \text{ cm}^{-3}$. P_i is the local gas pressure, with a pressure floor set proportional to gas density as $P \propto \rho_{\text{g}}^{4/3}$, normalized to a temperature of $T = 8 \times 10^3 \text{ K}$

at a hydrogen density of $n_{\text{H}} = 0.1 \text{ cm}^{-3}$. As such, dense star-forming gas is artificially pressurized in EAGLE, ensuring that the thermal Jeans length is always resolved, even at very high gas densities.

In GALFORM, the surface density of star formation in discs is linearly related to the surface density of molecular hydrogen, following empirical constraints from Blitz & Rosolowsky (2006). The total star formation rate is therefore linearly proportional to the star-forming ISM gas mass as

$$\psi = \nu_{\text{SF}} M_{\text{ISM,SF}}, \quad (\text{A4})$$

where $\nu_{\text{SF}} = 0.5$ is a constant empirically constrained from observations (Leroy et al. 2008; Bigiel et al. 2011; Rahman et al. 2012). Accordingly, the efficiency of star formation per unit star-forming ISM mass in galaxy discs is also constant. In merger or disc-instability triggered starbursts, nuclear gas is instead converted into stars following a decaying exponential function (Lacey et al. 2016).

A3 Disc angular momentum

In GALFORM, disc angular momentum is computed assuming that infalling gas from the halo conserves angular momentum (Cole et al. 2000). The total specific angular momentum of halo gas is set equal to that of the dark matter halo, with the radial specific angular momentum profile set assuming a constant rotation velocity. Within the disc, it is assumed that stars and gas always have equal specific angular momentum. There is also an assumption that disc specific angular momentum is unaffected by stellar feedback. Bulge/spheroid angular momentum is not explicitly modelled in GALFORM.

In EAGLE, the angular momentum of galaxies emerges naturally from locally solving for the laws of gravity and hydrodynamics.

A4 Stellar feedback

In EAGLE, each star particle represents a simple stellar population with a Chabrier (2003) stellar initial mass function (IMF). The gradual injection of mass and metals through stellar evolution back into the ISM is implemented as described in Wiersma et al. (2009). Type II SNe feedback occurs 30 Myr after a stellar particle forms. In the GALFORM model presented here, stars are also formed with a Chabrier (2003) IMF. Unlike EAGLE, GALFORM adopts the instantaneous recycling approximation, whereby all of the mass and metals returned to the ISM through stellar evolution are returned instantaneously as star formation takes place. Correspondingly, stellar feedback is assumed to occur simultaneously with star formation in GALFORM. The impact of this assumption in semi-analytic models is addressed by Yates et al. (2013), De Lucia et al. (2014), Hirschmann et al. (2016) and Li et al., (in prep).

Stellar feedback is implemented in EAGLE with the stochastic thermal energy injection scheme of the type introduced by Dalla Vecchia & Schaye (2008). This scheme is designed to minimise artificial radiative losses and instead allows the desired radiative losses to be set by hand by adjusting the amount of injected thermal energy (Schaye et al. 2015; Crain et al. 2015). Artificial losses are effectively suppressed by requiring that neighbouring gas particles heated by a supernova event are heated by $\Delta T = 10^{7.5} \text{ K}$,

well above the peak of the radiative cooling curve. The thermal energy injected into the ISM per SNe is set to $f_{\text{th}} 10^{51} \text{ ergs}$, where 10^{51} ergs is the canonical value for SNe explosions. The term f_{th} is parametrised as

$$f_{\text{th}} = f_{\text{th,min}} + \frac{f_{\text{th,max}} - f_{\text{th,min}}}{1 + \left(\frac{Z}{0.1 Z_{\odot}}\right)^{n_Z} \left(\frac{n_{\text{H,birth}}}{n_{\text{H,0}}}\right)^{-n_n}}, \quad (\text{A5})$$

where Z is the local gas metallicity and $n_{\text{H,0}}$ is the gas density that the stellar particle had when it formed. $f_{\text{th,min}}$ and $f_{\text{th,max}}$ are model parameters that are the asymptotic values of a sigmoid function in metallicity, with a transition scale at a characteristic metallicity, $0.1 Z_{\odot}$, and with a width controlled by n_Z . An additional dependence on local gas density is controlled by model parameters, $n_{\text{H,0}}$, and n_n . The two asymptotes, $f_{\text{th,min}}$ and $f_{\text{th,max}}$, are set to 0.3 and 3 respectively. In the low metallicity, high density regime, the energy injection therefore exceeds the canonical value for Type II SNe explosions by a factor 3. Crain et al. (2015) and Schaye et al. (2015) argue that this value is justified on both physical and numerical grounds (note also that the median energy injection value across the simulation is lower than unity Crain et al. 2015).

In GALFORM, rather than scale the efficiency of SNe feedback with local metallicity/gas density, the efficiency is defined and computed globally across each galaxy disc (and separately for galaxy bulges/spheroids). This efficiency is characterised by the dimensionless mass loading factor, β_{ml} , defined as the ratio of the mass-outflow rate (\dot{M}_{ejected}) from galaxies to the star formation rate (ψ). Note that this is a global quantity across a given galaxy and should not be compared to Eqn A5, which pertains to the local injection of energy at a given point in the ISM. In GALFORM, β_{ml} is explicitly parametrised as a function of galaxy circular velocity as

$$\beta_{\text{ml}} \equiv \frac{\dot{M}_{\text{ejected}}}{\psi} = \left(\frac{V_{\text{circ}}}{V_{\text{SN}}}\right)^{-\gamma_{\text{SN}}}, \quad (\text{A6})$$

where V_{SN} and γ_{SN} are model parameters that control the normalization and faint-end slope of the galaxy luminosity function (e.g. Cole et al. 2000) and V_{circ} is the galaxy circular velocity. For star formation taking place in discs, V_{circ} is set to the circular velocity of the disc at the radius enclosing half of the disc mass. For nuclear star formation taking place in galaxy bulges/spheroids, V_{circ} is correspondingly set equal to the circular velocity at the half-mass radius of the spheroid.

Unlike in EAGLE, the stellar feedback in GALFORM does not include any energetic considerations. While the thermal and kinetic energy of outflowing gas is not directly modelled in GALFORM, if we assume (as an example) that gas is launched from galaxies in a kinetic wind with a velocity of 250 km s^{-1} , we can estimate the galaxy circular velocity below which the energy injected exceeds the energy available. For the SNe parameters from our fiducial model ($V_{\text{SN}} = 380 \text{ km s}^{-1}$ and $\gamma_{\text{SN}} = 3.2$), and with a value of $8.73 \times 10^{15} \text{ erg g}^{-1}$ of energy available per unit mass turned into stars (as appropriate for a Chabrier IMF assuming 10^{51} erg per supernova and that stars with mass $6 - 100 M_{\odot}$ explode, Schaye et al. 2015), equating the (example) kinetic energy of the outflowing wind with the energy available yields that Eqn A6 violates energetic considerations below a circular velocity, $V_{\text{circ}} = 134 \text{ km s}^{-1}$. For our reference GALFORM model, this circular velocity corresponds to a halo mass, $M_{\text{H}} \approx 10^{12} M_{\odot}$ at $z = 0$. The corresponding mass-loading factor at this velocity is very large, $\beta_{\text{ml}} = 28$, significantly in excess of the values reported by simulations at this mass scale (e.g. Muratov et al. 2015; Christensen et al. 2016; Keller

et al. 2016). The mass-loading factors predicted by EAGLE will be presented in Crain et al. (in preparation) and we plan to explicitly compare these mass loading factors with GALFORM in future work.

A5 Black hole growth and AGN feedback

In EAGLE, SMBH seeds are placed at the position of the highest density gas particle within dark matter haloes of mass, $M_H > 10^{10} M_\odot/h$ (Schaye et al. 2015). Black holes then accrete mass with an Eddington limited, Bondi accretion rate that is modified if the accreted gas is rotating at a velocity which is significant relative to the sound speed (Rosas-Guevara et al. 2015). Black holes that are sufficiently close and with sufficiently small velocity are allowed to merge, forming a second channel of black hole growth.

Analogous to the implementation of stellar feedback, accreting SMBH particles stochastically inject thermal energy into neighbouring gas particles. The amount of energy injected per unit accretion contains a model parameter that controls the resulting relationship between SMBH mass and galaxy stellar mass, but not the effectiveness of AGN feedback (Booth & Schaye 2010; Schaye et al. 2015; Bower et al. 2017). This injection energy is stored in the black hole until it is sufficiently large to heat a neighbouring gas particle by $\Delta T = 10^{8.5}$ K which is an order of magnitude larger than the local heating from stellar feedback ($\Delta T = 10^{7.5}$ K).

In GALFORM, SMBHs are seeded inside galaxies when they first undergo a disc instability or galaxy merger event. SMBHs grow in mass primarily by accreting a fraction of the ISM mass converted into stars in starbursts that take place in galaxy bulges/spheroids during galaxy merger or disc instability events (Bower et al. 2006; Malbon et al. 2007). A second growth channel comes from black hole mergers, which take place whenever there is a merging event between two galaxies hosting black holes. We compare the GALFORM and EAGLE distributions of black hole mass as a function of stellar mass in Appendix E, where we show that GALFORM does not predict the steep dependence on stellar mass predicted by EAGLE at $z = 2, 4$.

The implementation of AGN feedback in GALFORM is fully described in Bower et al. (2006) (see also Lacey et al. 2016). The most salient parts of the modeling for this analysis are as follows. AGN feedback in GALFORM is implemented such that it can be effective only when the diffuse gas halo is in a quasi-hydrostatic state (Bower et al. 2006). This occurs when the radiative cooling timescale exceeds the gravitational freefall timescale in the diffuse gas halo. In this regime, it is assumed that a fraction of the diffuse infalling material is directly accreted onto the SMBH, forming a third growth channel. A fraction of the rest mass energy of this accreted material is assumed to be injected into the diffuse gas halo as a heating term. If this heating term exceeds the cooling rate, infall from the diffuse gas halo onto the ISM is assumed to be completely suppressed. As such, unlike in EAGLE, AGN feedback has no direct effect on gas in the ISM and does not drive galactic outflows.

A6 Gas return timescales

In GALFORM, gas which is ejected from galaxies is placed in a distinct reservoir. Gas is reincorporated from this reservoir back into the diffuse gas halo at a rate given by

$$\dot{M}_{\text{return}} = \alpha_{\text{return}} \frac{M_{\text{ejected}}}{\tau_{\text{dyn}}}, \quad (\text{A7})$$

where α_{return} is a model parameter (typically set close to unity

and set to 1.26 in our fiducial model), M_{ejected} is the mass in the ejected reservoir and τ_{dyn} is the halo dynamical time (Bower et al. 2006).

The spatial distribution of the ejected gas reservoir is not explicitly specified in GALFORM. Whether or not the ejected gas resides within or outside the virial radius has been subject to various interpretations as the model has evolved over time (Cole et al. 2000; Benson et al. 2003; Bower et al. 2006, 2012). Here, we choose the interpretation that the ejected gas is spatially located outside the halo virial radius for central galaxies. Physically, this corresponds to assuming that outflowing gas leaves the virial radius over a timescale that is short compared to other physically relevant timescales. For satellite galaxies, we consider ejected gas to be still within the virial radius of the host halo. This interpretation allows us to cleanly compare the indirect efficiency of feedback and the baryon cycle with EAGLE by measuring the fraction of baryons within the virial radius.

In EAGLE, no explicit gas return timescale is set, as the trajectories of gas particles are calculated self-consistently. In practice, the return times will be sensitive to the details of the implementations of supernova and AGN feedback, including the heating the temperatures.

A7 Radiative cooling and infall

In GALFORM, gas infalls from the diffuse gas halo onto the galaxy disc at a rate given by

$$\dot{M}_{\text{infall}} = \frac{4\pi \int_0^{r_{\text{infall}}} \rho_g(r) r^2 dr - M_{\text{cooled}}}{\Delta t} \quad (\text{A8})$$

where $\rho_g(r)$ is the so-called “notional” gas density profile, M_{cooled} is the mass that has already undergone infall from the notional gas profile onto the disc before the current timestep and Δt is the numerical timestep size (Cole et al. 2000). r_{infall} is the infall radius, which represents the radius within which gas has had sufficient time to infall from the notional profile to the disc. It is limited either by the gravitational freefall timescale or the radiative cooling timescale. r_{infall} is computed by equating the limiting radiative/freefall timescale with the time elapsed since the host halo last doubled in mass. This cooling model was introduced in Cole et al. (2000) and updated in Bower et al. (2006).

In EAGLE, gas infalls onto galaxies naturally as a consequence of hydrodynamics and gravity. Radiative cooling and photoheating are implemented element-by-element following Wiersma et al. (2009), assuming ionization equilibrium.

APPENDIX B: HALO MASS DEFINITIONS

Fig. B1 compares the DHALO halo masses used internally within GALFORM to the M_{200} halo masses measured from the reference hydrodynamical (top) and dark-matter-only (bottom) EAGLE simulations. The difference between these halo mass definitions leads to a small scatter between DHALO masses and M_{200} measured from the dark-matter-only simulation. There is also a small systematic offset at $z = 0$ (this offset only appears for $z < 1$) which has no trend with mass. The objects with much lower halo masses in GALFORM compared to the dark-matter-only simulation between $10^{13.5} < M_{200} M_\odot < 10^{14}$ are flagged as satellites by the DHALO algorithm but are considered central subhaloes by SUBFIND, leading to the large differences between halo masses. Comparing GAL-

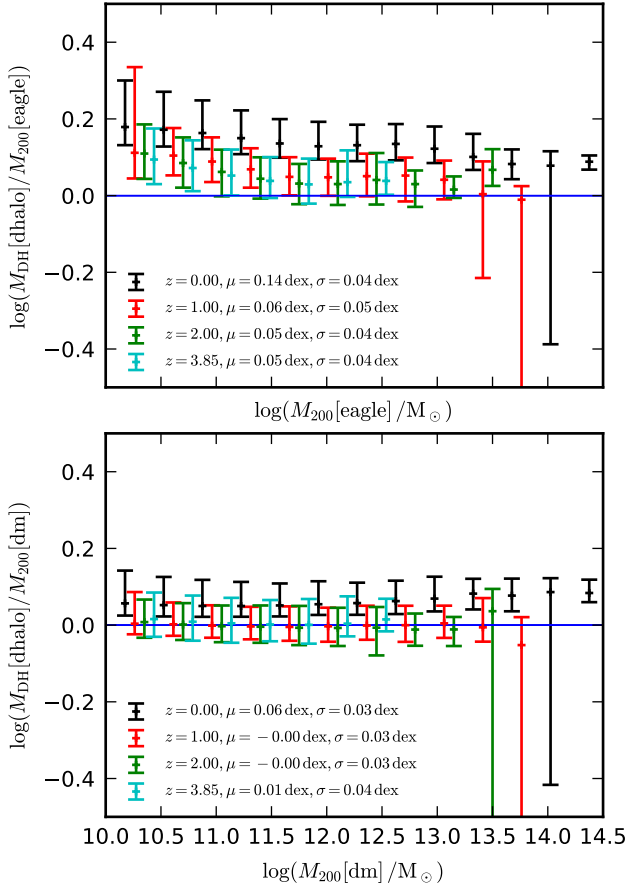


Figure B1. Comparison of halo masses between different definitions and simulations. *Top:* DHALO mass used internally within GALFORM, $M_{\text{DH}} [\text{dhalo}]$, compared to the halo mass, $M_{200} [\text{eagle}]$, (which includes baryons) measured from the reference EAGLE hydrodynamical simulation. *Bottom:* DHALO mass, $M_{\text{DH}} [\text{dhalo}]$, compared to the halo mass, $M_{200} [\text{dm}]$, measured from the EAGLE dark-matter-only simulation. Points show the 10, 50 and 90th percentiles of the distributions for a given redshift. Different point colours correspond to different redshifts, as labelled. Also labelled are the mean (logarithmic) vertical offset, μ , and the mean 1σ scatter.

FORM to the hydrodynamical simulation (top panel), the scatter is similar but with a larger, mass dependent, offset caused primarily by the ejection of baryons by feedback in EAGLE (see Schaller et al. 2015b, for a full analysis of this effect).

APPENDIX C: ISM DEFINITION IN EAGLE

In Section 2.6, we introduce selection criteria to define gas particles which belong to an ISM component in EAGLE. The canonical case demonstrating the behaviour of these selection criteria is shown in Fig. C1, which shows the criteria applied to a Milky-Way-like galaxy at $z = 0$. The top-left panel demonstrates the rotational support selection criteria defined by Eqn 3 and Eqn 4. For this galaxy, gas particles cleanly separate into two distinct populations (the ISM and a diffuse, ionized and hot gas halo). The middle-left panel shows the associated phase diagram, indicating that there is cool, rotationally supported ISM gas (cyan points) at low densi-

ties which is not forming stars. The lower-left panel shows radial mass profiles, splitting gas particles between neutral and ionized phases of hydrogen, following the methodology described in Lagos et al. (2015) and Crain et al. (2017), which utilises the self-shielding corrections from Rahmati et al. (2013). For this galaxy, our ISM definition includes almost all of the neutral hydrogen, as well as a small amount of amount of cool, rotationally supported, ionized hydrogen.

The right-panels in Fig. C1 show the spatial distribution of gas and stellar particles. A spiral structure for the ISM component is evident, with star-forming particles (yellow) tracing denser regions within the spiral arms compared to non-star-forming ISM particles (cyan). The circles in these panels relate to the various radial selection criteria described in Section 2.6. The black circle indicates twice the half-mass radius of the stellar component. Dense gas within this radius that is not considered to be rotationally supported can still be included within the ISM component. This is why there is a small number of ISM particles (yellow/cyan) outside the selection region in the upper-left panel of Fig. C1. The yellow circle in the right-panels indicates twice the radius enclosing 90% of the mass within the ISM. Gas particles outside this radius are then excluded from the ISM. In practice, this acts to remove a residual amount of distant, rotating material which is clearly not spatially associated to the ISM of the central galaxy. Removing this gas has minimal impact on our results. The green circle shows half the halo virial radius. Gas particles outside this radius are also excluded from the ISM. For this galaxy, this radius is significantly larger than the yellow circle and so is irrelevant.

While our ISM selection criteria appear to perform well for the galaxy shown in Fig. C1 (and we have checked a number of similar central/satellite examples for a variety of redshifts), other galaxies with more extreme properties pose a greater challenge. For passive, gas-poor galaxies, we find it is necessary to also remove gas particles from outside five times the radius enclosing half the stellar component. In passive galaxies, there is often no clear central ISM component in the radial profiles and most of the cool gas is in distant, rotating clumps. Including/excluding these clumps makes little difference for our analysis however because they form a negligible fraction of the mass in massive galaxies.

For massive, high-redshift star-forming galaxies the situation is more complex. Fig. C2 shows the same information as Fig. C1 but for the “worst-case” scenario of a massive ($M_* = 10^{11} M_\odot$), star-forming ($SFR = 100 M_\odot \text{ yr}^{-1}$) galaxy at $z = 2$. This galaxy is an extreme example for which there is no apparent bimodality between a rotationally supported ISM and a diffuse, hot, halo. Rather, the gas appears to be dynamically disturbed, with a very broad mass distribution in the upper-left panel of Fig. C2. The 1σ mass contour (white) encloses gas which is not considered to be in rotational equilibrium and includes a mix of hot and cool diffuse gas as well as a residual amount of cold, dense, radially infalling gas (red and green points). The 2σ contour encloses a significant amount of star-forming gas which is not considered part of the ISM (green points), either because it is rotating too slowly or too quickly or because it has too high a radial velocity to be in dynamical equilibrium. The ISM material that is selected by the criteria described in Section 2.6 is either rotationally supported (and typically spatially extended) or is centrally-concentrated and is supported by a combination of thermal pressure and rotation (yellow points to the left of the rotationally supported selection region in the upper left panel). The relative contributions from these two components to the total ISM are roughly equal. Given the dynamically disturbed nature of this system, it is unclear whether the rotational equilibrium crite-

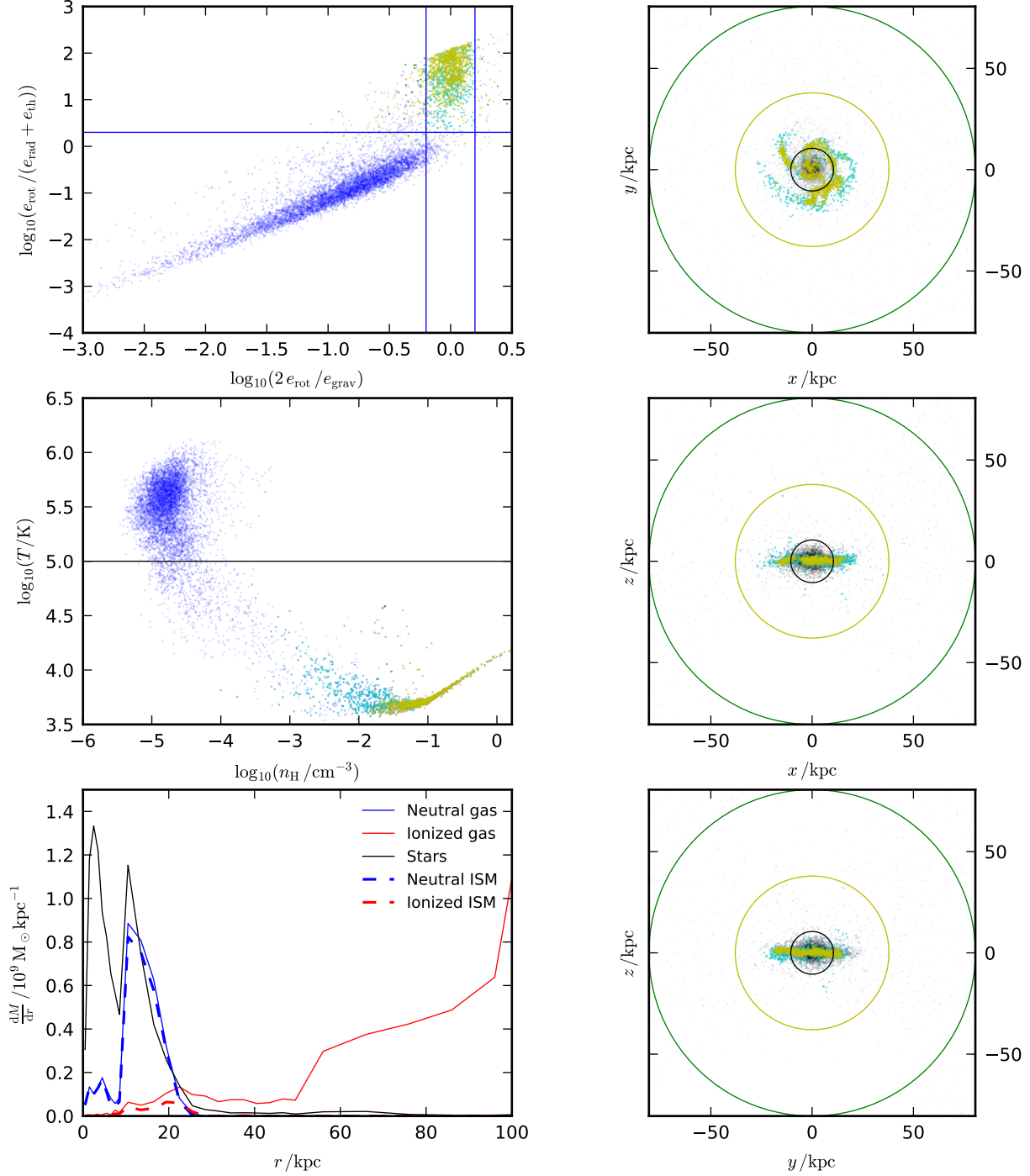


Figure C1. Diagnostic information for selecting the ISM in a central, star-forming spiral galaxy with $M_{\star} = 10^{10} M_{\odot}$ at $z = 0$. Coloured points show individual gas particles associated to the central subhalo, with yellow indicating star-forming ISM, cyan indicating non-star-forming ISM and small blue points indicating non-ISM particles. Black points show stellar particles. *Top-left:* Rotational support selection criteria. Particles above the horizontal line and between the vertical lines are considered rotational supported. *Middle-left:* Phase diagram. The horizontal line shows the temperature cut, above which gas is excluded from the ISM unless it has a density, $n_{\text{H}} > 50 \text{ cm}^{-3}$. *Bottom-left:* Radial mass profiles of stars (black), neutral gas (neutral hydrogen and associated helium, solid blue), neutral ISM (dashed blue), ionized gas (solid red) and ionized ISM (dashed red). *Right-panels:* Spatial distributions of gas and stellar particles in three projections that are face-on (top) and edge-on (middle and bottom). Non-ISM and stellar particles are only shown within a 80 pkpc slice along the line-of-sight axis for clarity. The black circles show twice the half-mass radius of the stellar component. The yellow circles show twice the radius containing 90% of the pre-selected ISM mass. Green circles show half of the halo virial radius.

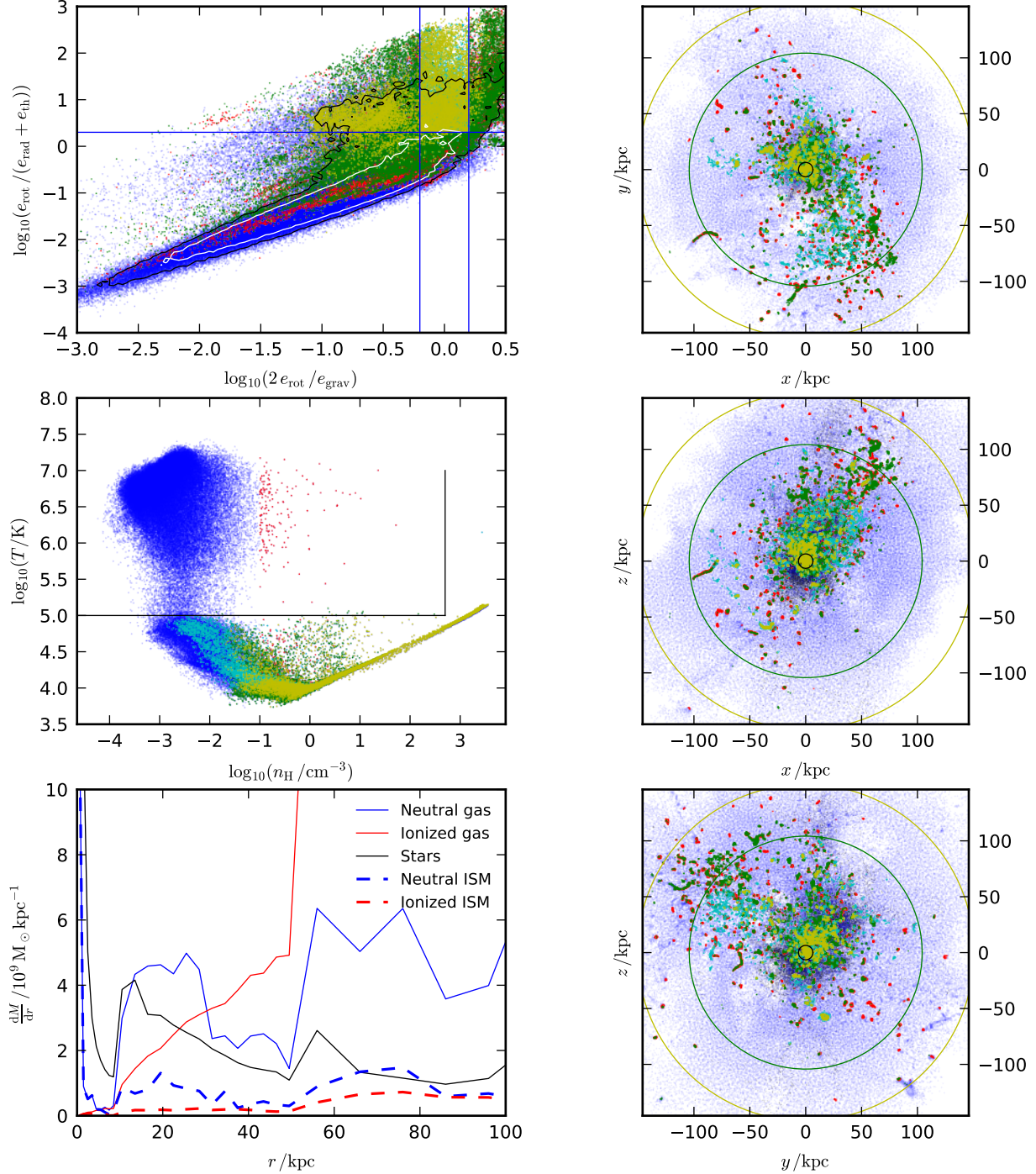


Figure C2. Diagnostic information for selecting the ISM in a central, highly star-forming galaxy with $M_* = 10^{11} M_\odot$ at $z = 2$. Panel information as well as point and line formatting follow Fig. C1, with the following additions. Red points show gas particles that are dense ($n_H > 0.1 \text{ cm}^{-3}$) but are not considered part of the ISM. Green points (over plotted) show gas particles that are star-forming but not considered part of the ISM. In the upper-left panel, contours are shown that enclose 90 % (black) and 68 % (white) of the total gas mass.

ria used to select the spatially extended ISM in this case are truly robust. However, the majority of the spatially-extended neutral hydrogen which is not included in the ISM is excluded because it is radially infalling and as such is robustly excluded.

The contrast between the situations presented in Fig. C1 and Fig. C2 serves to highlight the difficulty of defining the ISM across

all galaxies with a uniform set of selection criteria. Nonetheless, simply selecting star-forming gas particles would cut away 30 % of the mass and 40 % of the angular momentum in the case of the well-defined ISM shown in Fig. C1. Taking gas within an aperture is also likely to be overly simplistic. Too small an aperture will cut away spatially extended, high-angular-momentum gas. Too large an aper-

ture (even with a temperature cut) will select significant amounts of radially infalling gas around high-redshift galaxies that should not (at least according to our physical criteria) be considered as part of the ISM.

To assess the global behaviour of our criteria, Fig. C3 shows the resulting ISM gas fractions as a function of stellar mass for three redshifts. These are then compared to the total gas within 30 pkpc and the neutral hydrogen within 30 pkpc, which is taken as a proxy for the ISM in Lagos et al. (2015). At $z = 0$, the resulting gas fractions are similar, indicating that the most of the hydrogen within 30 pkpc of the halo centre is in a neutral phase and is in dynamical equilibrium. At $z = 2$, our ISM definition is very close to taking neutral hydrogen within 30 pkpc but the total gas fractions (black lines) are significantly higher, presumably because of the impact from supernova feedback in heating circumgalactic gas around high-redshift galaxies. At $z = 3.85$, our ISM definition yields systematically lower gas fractions than taking neutral gas within an aperture, presumably by excluding neutral hydrogen present in dense, radially infalling accretion streams.

APPENDIX D: GALAXY SIZES

Fig. D1 shows the galaxy size distributions as a function of stellar mass for EAGLE and GALFORM. As discussed in Guo et al. (2016), the most obvious tension between the models is that GALFORM predicts very compact sizes for massive galaxies. The exact underlying cause for these compact sizes is presently unclear as it is challenging to disentangle the combined effects of modelling adiabatic halo contraction, the calculation of pseudo-angular momentum after galaxy mergers/disc instabilities and the impact of the angular momentum histories of progenitor galaxy discs (Cole et al. 2000). Any of these areas of the modelling could be suspect. We defer further exploration of this problem in GALFORM to future work.

Also apparent in Fig. D1 is that the scatter in galaxy size at a fixed stellar mass is significantly larger in GALFORM than in EAGLE, and that the sizes of low-mass galaxies are larger in GALFORM than in EAGLE. We do not address the former discrepancy in this paper. The latter discrepancy is explored in Section 5 where we show that assuming that star-forming gas has the same specific angular momentum as the total ISM reservoir likely leads to erroneously high specific stellar angular momentum (and hence galaxy sizes) in disc-dominated (low mass, low redshift) galaxies.

Fig. D1 also shows observational data from the GAMA survey (Baldry et al. 2012) and the CANDELS survey (van der Wel et al. 2014). For GAMA, two samples of red and blue galaxies are presented and the sizes quoted are effective radii in the i band. For CANDELS, two samples of star-forming and passive galaxies (determined from rest-frame colour distributions) are presented and the sizes quoted are the semi-major axes of 1D Sersic fits at a rest-frame wavelength of 5000 Å. Note that we do not attempt to correct for inclination effects for sizes presented from EAGLE and GALFORM. While the comparison of these observed distributions to the models should be interpreted with care because of sample selection, projection and mass-to-light ratio effects, it is nonetheless clear that EAGLE predicts a more realistic size-mass distribution than GALFORM, particularly in the local Universe (where EAGLE was calibrated to predict realistic sizes).

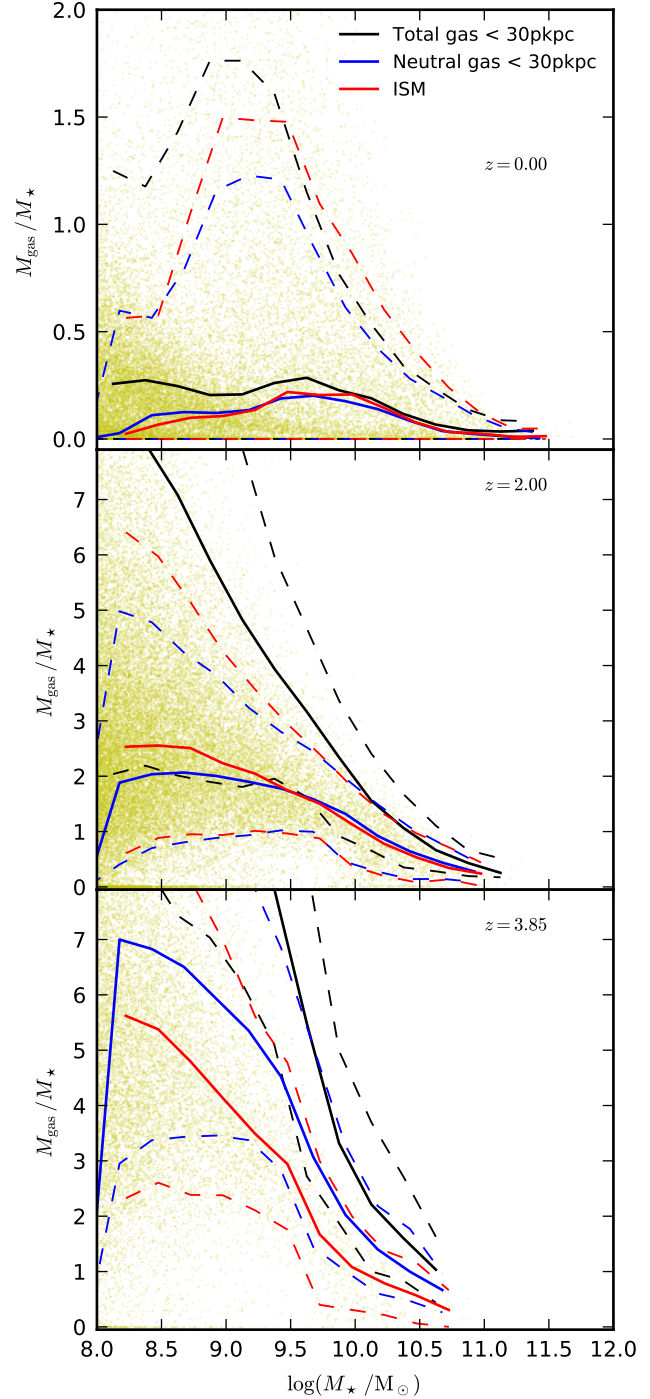


Figure C3. Comparison of different possible definitions of the ISM for galaxy gas fractions. Red lines show the distributions when using the ISM definition defined in Section 2.6. Blue points show the corresponding distributions when taking all neutral hydrogen (and associated helium) with a 30 pkpc aperture. Black points show the distributions when taking all gas within a 30 pkpc aperture. Solid lines show the medians and dashed lines show the 16 and 84th percentiles of the distributions.

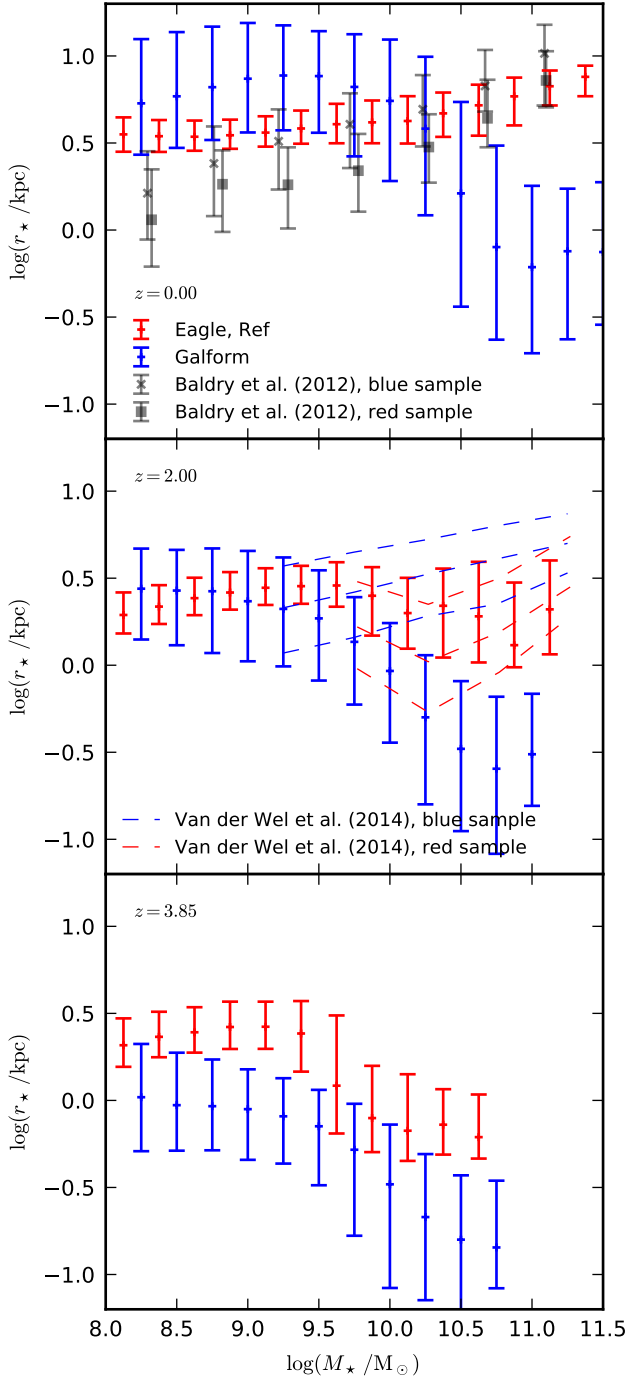


Figure D1. Galaxy size distributions as a function of stellar mass. Sizes, r_* , from the reference GALFORM (blue) and EAGLE (red) models are defined as the 3D radius enclosing half of the stellar mass (within a 30 pkpc aperture for EAGLE). The points and errorbars show the 16, 50 and 84th percentiles of the distributions. Grey points and errorbars show the corresponding distribution from the GAMA survey, as presented in Baldry et al. (2012). Grey crosses and squares correspond to samples of blue and red galaxies respectively. Blue and red dashed lines show respectively the distributions for blue and red galaxy samples from the CANDELS survey, as presented in van der Wel et al. (2014). Each panel corresponds to a different redshift, as labelled.

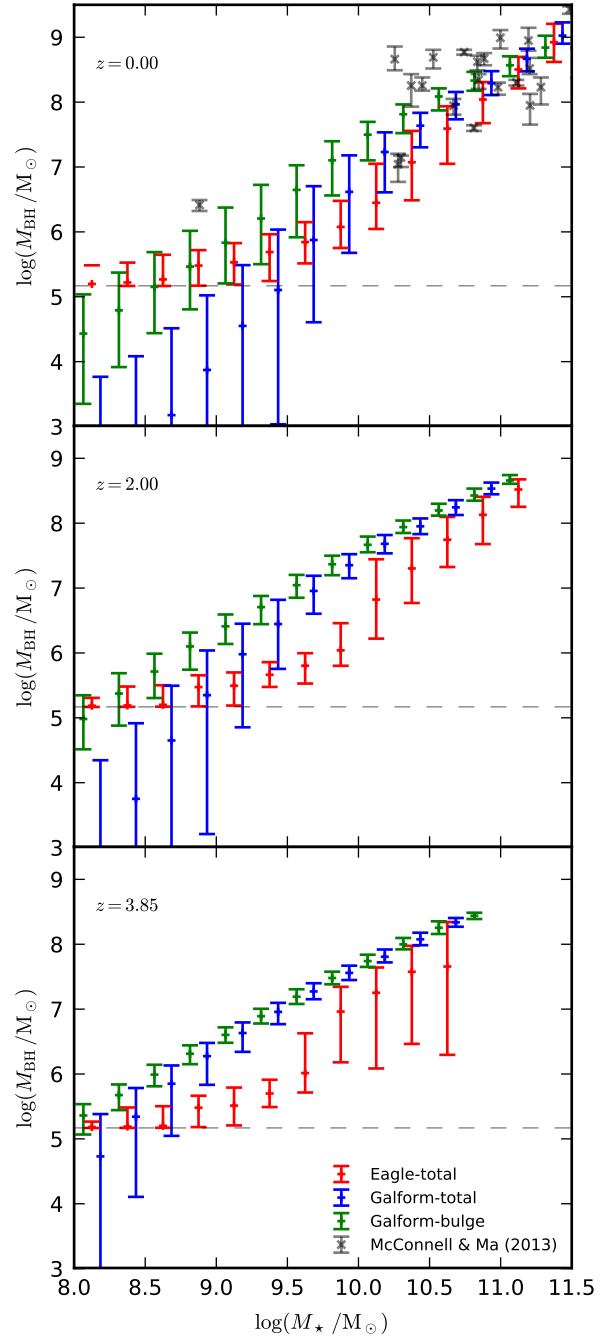


Figure E1. Black hole mass as a function of stellar mass. Red and blue points show the distribution as a function of total stellar mass from EAGLE and GALFORM respectively. Green points show the distribution as a function of bulge mass from GALFORM. These points and errorbars show the 16, 50 and 84th percentiles of the distributions. Black points show the compilation of observations from McConnell & Ma (2013), which are plotted as a function of bulge mass rather than total stellar mass. Dashed grey horizontal lines indicate the black hole seed mass in EAGLE. Each panel corresponds to a different redshift, as labelled.

APPENDIX E: BLACK HOLE MASSES

Fig. E1 shows the relationship between SMBH mass and stellar mass in the two models. At $z = 0$, the two models are very similar for $M_* > 10^{10} M_\odot$. For $9 < \log(M_*/M_\odot) < 10$, GALFORM predicts a significantly larger scatter in SMBH mass. Unlike in EAGLE, in GALFORM black hole growth is explicitly coupled to the growth of the galaxy bulge. The large scatter therefore reflects the significant scatter in bulge-to-total stellar mass ratio predicted by GALFORM in this mass range. The fraction of bulge stars that were formed quiescently in progenitor discs (versus bulge stars that were formed in galaxy merger or disc instability triggered star bursts) also plays a role in shaping the scatter in SMBH mass. At lower masses, EAGLE is affected by the seed mass, rendering a comparison meaningless.

Interestingly, at higher redshifts EAGLE predicts lower black hole masses compared to GALFORM, and a much steeper dependence with stellar mass at high masses. This effect is discussed extensively in Bower et al. (2017), who interpret SMBH growth in EAGLE as governed by a strongly non-linear transition in SMBH accretion efficiency that occurs at a characteristic halo mass scale. This scale is associated with the scale at which a hot corona develops, preventing SNe from driving a buoyant outflow. By construction, a strongly non-linear accretion efficiency transition does not emerge in GALFORM, leading to a shallower SMBH-stellar mass relation.